

# A Study of the Iceland–Faeroe Frontal Variability Using the Multiscale Energy and Vorticity Analysis

XIANG SAN LIANG

*Division of Engineering and Applied Sciences, Harvard University, Cambridge, Massachusetts*

ALLAN R. ROBINSON

*Division of Engineering and Applied Sciences, and Department of Earth and Planetary Sciences, Harvard University, Cambridge, Massachusetts*

(Manuscript received 20 October 2003, in final form 24 May 2004)

## ABSTRACT

The multiscale nonlinear interactive Iceland–Faeroe frontal (IFF) variability during 14–22 August 1993 is investigated for complex dynamics with the localized multiscale energy and vorticity analysis (MS-EVA). In terms of multiscale window transform, the cold meandering intrusion observed in the IFF experiment is represented on a mesoscale window. The resulting mesoscale energetics for the deep layer show an isolated center of transfer of potential energy from the large-scale window into the mesoscale window in the study domain. This large-to-mesoscale potential energy transfer, or BC for short, is a baroclinic instability indicator by the MS-EVA-based stability theory. Signatures on other energetics maps and the reconstructed mesoscale structures all support this baroclinic instability. On the BC map, the transfer hotspot originally resides near the western boundary. It travels along the front into the interior domain in a form of convective instability and then, on 19 August, changes into another instability that is absolute in character. Correspondingly, disturbances switch from a spatial growing pattern into a time growing mode, culminating on 21 August, the day just before the intrusion matures. The whole process lasts for about five days, limited within a small horizontal region and beneath a depth of approximately 150 m. By interaction analysis, the energy locally gained from this process goes to the submesoscale window as well, but most of it remains in the mesoscale window, serving to fuel the growth of the meandering intrusion.

## 1. Introduction

We present a dynamical study of the nonlinear meandering of the Iceland–Faeroe front (IFF) with a dataset collected during August 1993 by NRV *Alliance*. Dynamical processes are elucidated in terms of a novel methodology applicable to complex systems with multiple interactive scales in time and space. This study has been carried out not only because of our interest in the IFF physics, but also to demonstrate the capability of this new methodology in handling multiscale, highly nonlinear, and intermittent and episodic events.

### *a. The Iceland–Faeroe frontal variability*

The IFF is a zone of abrupt change in temperature and salinity along the ridge between Iceland and the Faeroe Islands. Defined either as the 2°–7°C gradient or the 35-psu isohaline (see Hansen and Meincke 1979),

it separates the the cold fresh Arctic waters from the warm saline waters in the North Atlantic (cf. Fig. 1). The intense alongfront upwelling, the energetic current system, and accordingly the sound speed variation have made the IFF a region of commercial and military interests, as well as oceanographic importance. For a historical account of the research for this area, refer to Hopkins (1988) and Robinson et al. (1996) and the references therein.

The IFF system is highly variable, and the variability appears in the form of meandering and intrusions. Heat and salt are transported across the front, making the IFF variability an important mechanism of communication between the two major oceans. Research along this line has been active for a long time. Recent work includes, for example, Willebrand and Meincke (1980), Hallock (1985), Allen et al. (1994), and Miller et al. (1995). During 14–23 August 1993, a highly resolved hydrographic dataset was acquired within the inset box of Fig. 1 by Harvard University in cooperation with North Atlantic Treaty Organisation (NATO) Supreme Allied Commander, Atlantic (SACLANT) Undersea Research Center during the NRV *Alliance* cruise (Robinson et al.

---

*Corresponding author address:* X. San Liang, Harvard University, Pierce Hall G2H, 29 Oxford Street, Cambridge, MA 02138.  
E-mail: liang@deas.harvard.edu

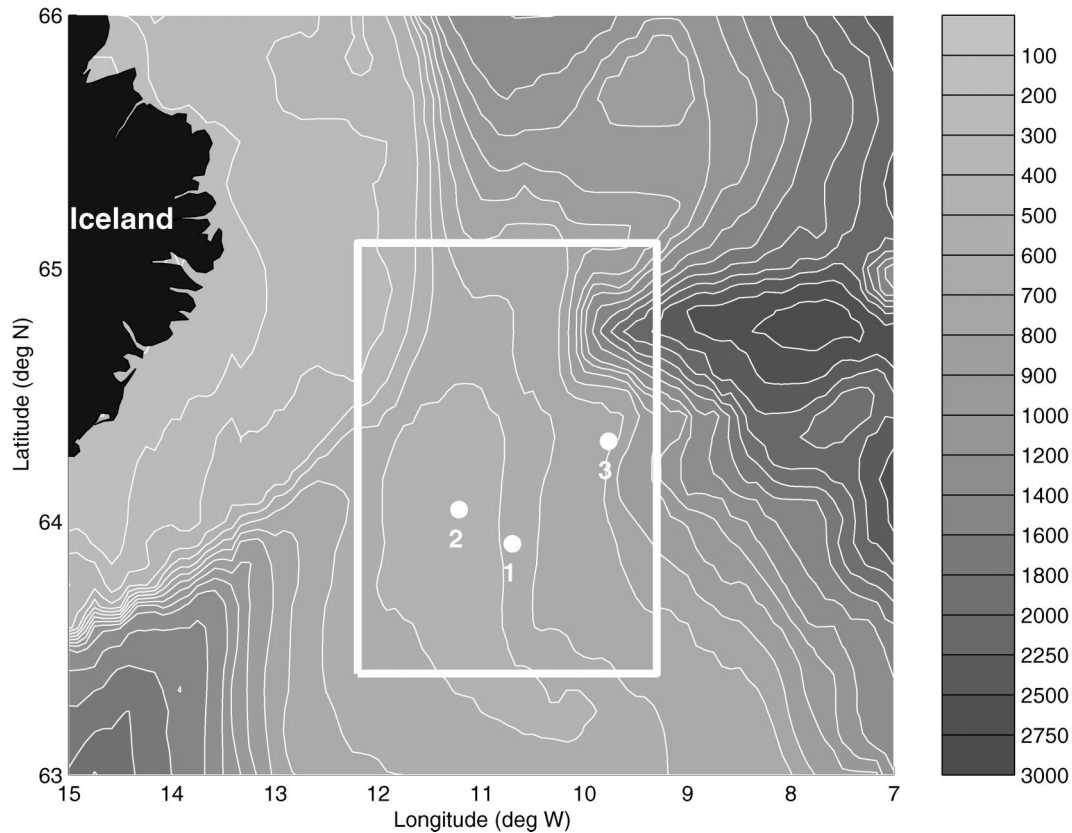


FIG. 1. Bottom topography of the IFF region (depth in meters). Shown in the box is the experimental domain, which in the model is discretized into a grid with  $57 \times 77$  mesh points. The three points mark the locations of the point time series for spectral analysis. They are located, in grid index pairs, at 1: (30, 24), 2: (20, 30), and 3: (48, 42).

1996; Miller and Cornuelle 1999; Liang 2002). The observed temperature objectively mapped for 15, 19, and 22 August is shown in Figs. 2a–c, from which we see an apparent cold tongue intrusion on 22 August 2003. The sea surface temperature from the satellite picture reconfirms this observation (Fig. 2d). In this study we

want to investigate how the front meanders and what mechanism is underlying the intrusion.

The IFF variability could be either driven by external forcing or due to internal dynamics. Contribution from atmospheric pressure or wind stress is generally inconsequential. It is at least one order of magnitude smaller

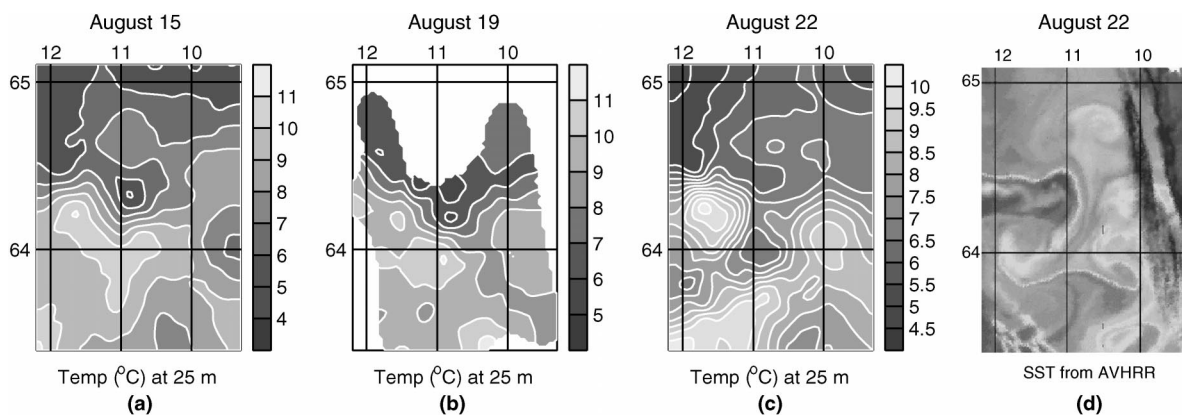


FIG. 2. (a)–(c) OA maps of the observed temperature for 15 Aug (day 1), 19 Aug (day 5), and 22 Aug (day 8) 1993, which represent the initialization survey, zig-zag survey, and validation survey, respectively. The axes are in longitudes ( $^{\circ}$ W) and latitudes ( $^{\circ}$ N). In (b), only the region with tolerable errors ( $\leq 25\%$  of the maximal variance) is shown. (d) A satellite infrared image (AVHRR) for the sea surface temperature of the model domain on 22 Aug (adapted from Robinson et al. 1996).

TABLE 1. Symbols for multiscale energetics (time step  $n$ , window  $\varpi$ )

Kinetic energy (KE)		Available potential energy (APE)	
$\dot{K}_n^\varpi$	Time rate of change of KE	$\dot{A}_n^\varpi$	Time rate of change of APE
$\Delta Q_{K_n^\varpi}$	KE advective working rate	$\Delta Q_{A_n^\varpi}$	APE advective working rate
$T_{K_n^\varpi, h}$	KE transfer due to horizontal flow	$T_{A_n^\varpi, h}$	APE transfer due to horizontal gradient of $\rho$
$T_{K_n^\varpi, z}$	KE transfer due to vertical flow	$T_{A_n^\varpi, z}$	APE transfer due to vertical gradient of $\rho$
$-b_n^\varpi$	Rate of buoyancy conversion	$b_n^\varpi$	Rate of inverse buoyancy conversion
$\Delta Q_{P_n^\varpi}$	Pressure working rate	$TS_{A_n^\varpi}$	APE transfer due to $\partial\bar{p}/\partial z$

than the eddy potential energy obtained from instabilities in the estimates by Willebrand and Meincke (1980), Allen et al. (1994), and Killworth et al. (1984). This intrinsic mechanism assertion has been further verified by energy diagnosis. Miller et al. (1995) found on their energy and vorticity analysis (EVA) maps of a quasi-geostrophic model a signature of finite-amplitude baroclinic instability from a hydrocast survey acquired in October 1992.

The August 1993 IFF variability seems to be also driven by internal dynamics. This is based on the successful prediction of the observed events in the shipboard real-time forecast, which does not take into account the wind stress and atmospheric pressure (Robinson et al. 1996). A faithful investigation of the underlying dynamics, however, is difficult with traditional methodologies because of the nonlinearity, the different scales involved, the time intermittency, and motile spatial localization. In this study, we will see how a new methodology, the multiscale energy and vorticity analysis, provides a satisfactory solution.

#### b. Multiscale energy and vorticity analysis (MS-EVA) and the MS-EVA-based localized stability analysis

The multiscale energy and vorticity analysis is a new methodology for the investigation of multiscale interactive oceanic processes that are intermittent in space and time. It is real problem-oriented and is objective in nature. Through exploring pattern generation and energy and enstrophy transfers, transports, and conversions, it helps to unravel the intricate relationships between events on different scales and locations in phase and physical spaces. The basic idea is delineated and the formulation is developed in Liang and Robinson (2003a, hereinafter LR1), and an avenue to application is established in Liang and Robinson (2003b, hereinafter LR2). Also established in LR2 is a generalization of the concept of stability on a localized basis, which allows one to build an easy-to-use criterion for the identification of baroclinic and barotropic instability processes for real ocean and atmosphere datasets.

In the MS-EVA, processes are represented on scale windows. By a *scale window* we mean a subspace of the space to which the field under consideration belongs, with a certain range of scales involved. The range is delimited by scales in the spirit of orthonormal wavelet analysis and is expressed in scale levels (cf. LR1; Kumar

and Foufoula-Georgiou 1997). A scale level  $j$  is a dimensionless index such that  $2^{-j}$  measures the passage of events since the beginning for a time series scaled by its duration. For the IFF process, we particularly need three scale levels,  $j_0, j_1$ , and  $j_2$ ,  $j_0 \leq j_1 \leq j_2$ , that demarcate three mutually exclusive windows: 1) large-scale window ( $j \leq j_0$ ), 2) mesoscale window ( $j_0 < j \leq j_1$ ), and 3) submesoscale window ( $j_1 < j \leq j_2$ ). For simplicity, a window may be referenced as  $\varpi$ , with  $\varpi = 0, 1, 2$  standing for large scale, mesoscale, and submesoscale, respectively. The MS-EVA provides a way to study the interactions between these windows.

We will use the multiscale energetics of the MS-EVA for the present study. In a symbolic form, the growths of kinetic energy ( $K_n^\varpi$ ) and available potential energy ( $A_n^\varpi$ ) on window  $\varpi$  ( $\varpi = 0, 1, 2$ ) and at time step  $n$  for a frictionless fluid flow are governed by

$$\dot{K}_n^\varpi = \Delta Q_{K_n^\varpi} + \Delta Q_{P_n^\varpi} + T_{K_n^\varpi} - b_n^\varpi \quad \text{and} \quad (1)$$

$$\dot{A}_n^\varpi = \Delta Q_{A_n^\varpi} + T_{A_n^\varpi} + b_n^\varpi, \quad (2)$$

where the  $\Delta Q$  terms represent transport processes in physical space, and the “ $T$  terms”

$$T_{K_n^\varpi} = T_{K_n^\varpi, h} + T_{K_n^\varpi, z} \quad \text{and} \quad (3)$$

$$T_{A_n^\varpi} = T_{A_n^\varpi, h} + T_{A_n^\varpi, z} + TS_{A_n^\varpi} \quad (4)$$

are *perfect transfers* among scale windows in the sense that they vanish when averaged over windows  $\varpi$  and time steps  $n$ . In the equations, the symbol  $(\cdot)_n^\varpi$  indicates a multiscale window transform (LR1, section 2) on time window  $\varpi$  and at times  $n$ . Other notations are summarized in Table 1. Note all these terms are horizontally treated with a two-dimensional large-scale window synthesis (LR1, section 7).

Perfect transfer is a key concept in the MS-EVA formulation (LR1). It allows one to separate transport processes from the nonlinear energetics terms based on a firm physical ground and, hence, to tell whether the energy growth for a window at a particular location and time is due to the local energy transfer or transport from surrounding regions. We have established rigorously that these  $T$  terms are closely related to the classical geophysical fluid dynamics (GFD) stability (LR2), and the classical hydrodynamic stability theory in the sense of Lyapunov (Liang 2004, manuscript submitted to *J. Fluid Mech.*). A natural generalization of these stability theories to handle real world problems is fulfilled with these

terms. In the simple case with only two windows (window 0 and window 1), let

$$BC = T_{A_h}^{0 \rightarrow 1} = T_{A_h, h}^{0 \rightarrow 1} + T_{A_h, z}^{0 \rightarrow 1} + TS_{A_h}^{0 \rightarrow 1}, \quad (5)$$

where the superscript  $0 \rightarrow 1$  is an interaction analysis operator that selects out the large-scale-to-mesoscale transfer component (see LR1, section 9), and

$$BT = T_{K_h}^{0 \rightarrow 1} = T_{K_h, h}^{0 \rightarrow 1} + T_{K_h, z}^{0 \rightarrow 1}. \quad (6)$$

A criterion was derived in LR2 for instability identification:

- 1) a flow system is locally unstable if  $BT + BC > 0$ , and vice versa;
- 2) for an unstable system, if  $BT > 0$  and  $BC \leq 0$ , the instability the system undergoes is barotropic;
- 3) for an unstable system, if  $BC$  is positive but  $BT$  is not, then the instability is baroclinic; and
- 4) if both  $BT$  and  $BC$  are positive, the system must be undergoing a mixed instability.

For convenience,  $BC$  and  $BT$  may be referred to as, respectively, baroclinic instability indicator and barotropic instability indicator, though neither of them alone is enough for instability identification. All the above terms are local in time and space, and hence the criterion is applicable to problems on a generic basis.

### c. Outline of this study

The objective of this study is to diagnose the IFF variability using the MS-EVA and the MS-EVA-based localized stability analysis and to investigate how the front meanders, evolves, and intrudes. The whole study is based on a numerical simulation, which is reviewed in the following section. The diagnosis begins in section 3 with a scale analysis of the IFF variability, which is used to determine the time and scale window bounds needed for the process decomposition. The application of MS-EVA is set up in section 4. Dynamical processes are identified and analyzed (section 5), with the localized stability theory developed in LR2, which is further supported with evidence from mesoscale energetic balances (section 6) and reconstructed structures (section 7). In section 8, we show that the process identified is, indeed, the cause of the variability. This study is summarized and concluded in section 9.

## 2. An overview of the 1993 IFF variability simulation

The August 1993 IFF dataset, unprecedented in its time and space resolution, has captured several crucial moments of how a cold-tongue “deep-sock” meander was formed. The research domain that it covers is centered at  $64.25^\circ\text{N}$ ,  $10.75^\circ\text{W}$  and extends 140 km zonally and 190 km meridionally (Fig. 1). The whole cruise comprises an initialization survey (14–16 August), an adaptive sampling (zig-zag) survey (18–20 August), and

TABLE 2. Parameters for the application of MS-EVA.

Parameters	Value
Time window bounds $j_0, j_1, j_2$	3, 5, 10 (2.7, 0.7, 0.02 days)
Space window bounds	
$j_0^{\text{sp}}$	5 (~25 km)
$\bar{\rho}(z), s, d \log s / dz$	See Fig. 8
Grid	$57 \times 77 \times 9$
Time step size $\Delta t$	1800 s
Horizontal grid spacing $\Delta x, \Delta y$	2.5 km
Vertical grid spacing $\Delta z$	
Level 1 (at depth 7.5 m)	15 m
Level 2 (25.0 m)	20 m
Level 3 (47.5 m)	25 m
Level 4 (80.0 m)	40 m
Level 5 (125.0 m)	50 m
Level 6 (190.0 m)	80 m
Level 7 (300.0 m)	140 m
Level 8 (500.0 m)	260 m
Level 9 (780.0 m)	300 m

a validation survey (20–23 August). The initialization survey is used to initialize the model, and the validation survey is reserved for validation only. The zig-zag survey, which, in the time available adaptively sampled the subjectively identified region of strong dynamical evolution, provides updating data. Let 14 August be day 0, 15 August be day 1, and so forth (Robinson et al. 1996). The temperature objectively mapped at the 25-m level in Figs. 2a–c is thus for day 1, day 5, and day 8. Initially the fresh cold Arctic waters are well separated from the warm salty Atlantic waters. The front appears as an rectangular meander on day 1. By 19 August (day 5), its left side has straightened toward the southeast, and the whole axis is in a triangular form. The strong south-eastward flow has been verified by drifter trajectories (Robinson et al. 1996). Following this reorientation of the front there is a meander, and a deep intrusion develops (20–23 August). This cold intrusion has been described by its geometry as “deep sock” (Robinson et al. 1996) or “hammerhead” (Miller and Cornuelle 1999). It is also apparent on the satellite infrared image [Advanced Very High Resolution Radiometer (AVHRR)] of the sea surface temperature (SST). In Fig. 2d, the general pattern of the intrusion actually looks like a T with upper side down, oriented toward the southeast, with some warm water injected into the north. Superimposed on this pattern we also see features of smaller scales, thanks to the high resolution. These details reveal to us a SST image that is rich in self-similarities, implying the possible role of strong nonlinearity in the frontal meandering process.

Liang (2002, chapter 5) used these snapshots to reconstruct pictures for the whole process. The research domain is discretized uniformly in  $x$  (longitudinal) and  $y$  (latitudinal) into 57 and 77 grid lines, respectively ( $\Delta x = \Delta y = 2.5$  km). In the vertical direction, the grid has nine levels, with the top five being flat  $z$  levels, and the four below terrain-following sigma levels (cf. Table 2).

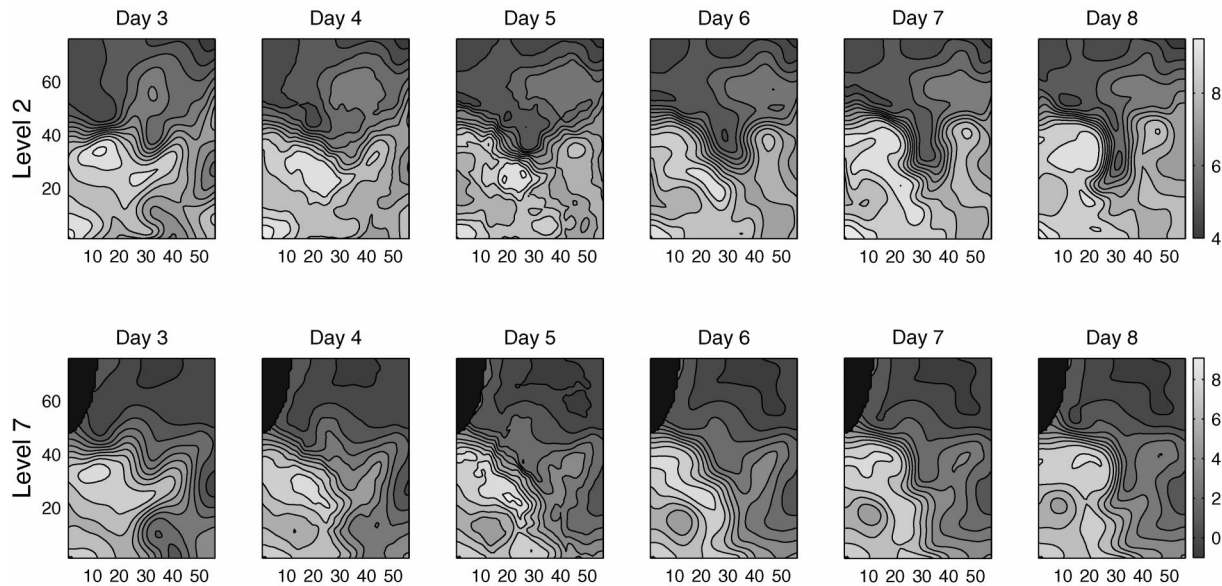


FIG. 3. A time sequence of the simulated posterior temperature (units:  $^{\circ}\text{C}$ ) at depth 25 m (level 2) and depth 300 m (level 7) from day 3 (17 Aug) through day 8 (22 Aug). Data are assimilated on days 1, 2, 4, and 5 at noon with weights 1.0, 1.0, 0.5, and 1.0, respectively. The  $x$  and  $y$  axes are the grid indices  $I$  and  $J$ .

Following the strategy of Robinson et al. (1996), Liang carried out a simulation with the observation data sequentially assimilated when they become available. The assimilation is fulfilled using a pointwise optimal interpolation, with the error field from the objective analysis. It is performed daily on days 1, 2, 4, and 5, each time at 1200 local time. The day-1 and day-2 updates, which complete the initialization, both use weight 1.0, while on days 4 and 5 the zig-zag data are assimilated in a ramp-up way (with weights 0.5 and 1.0). [See Liang (2002) for details.] Figure 3 is the simulated temperature (posterior) time sequence showing the evolution and the formation of the cold-tongue meandering intrusion (days 6, 7, 8). Consider the morphogenesis of the front at 25 m. Initially, the front is generally west–east oriented. It then straightens toward southeast, resulting in an axis in a V shape. This is the reorientation observed on day 5. After that, the western part of the front begins to crest and, eventually, gives way to a tonguelike geometry. We will refer to the frontal shape on day 8 as the “mature phase” of the meandering, as by this time the meander has shifted its southeastward orientation to the southwest, and after this day it begins to disappear (figures not shown).

It merits mentioning that the intrusion has a distinct vertical structure. Shown in the bottom row of Fig. 3 is a time sequence of the temperature for the 300-m level. One observation is that of the phase difference between these two layers. Comparing the positions of the meander in the top row and bottom row, it is seen that the surface layer lags the deep layer in the development of the meander. In reproducing this vertical

structure, both grid resolution and appropriate assimilation of the zig-zag data have been found important.

As a preliminary analysis, we compute the buoyancy conversion rate,  $b = (g/\rho_0)w\rho$ , a quantity that has been used frequently in geophysical fluid dynamics diagnostics. Presented in Fig. 4, is a sequence of  $b$  for depth 300 m, from 19 August (day 5) until the meander matures (day 8). Apparently, there exists conversion between kinetic energy (KE) and available potential energy (APE), but the conversion evolution does not correspond well in location to the cold tongue. Moreover,  $b$  rarely takes negative values in the neighborhood of the meandering region. (Only in a narrow region in the northeast is  $b$  smaller than zero.) That is to say, instead of being released to feed the meandering growth, APE drains KE in most of the intrusion area. The counter-intuitivity of Fig. 4 shows the difficulty of traditional energy diagnosis in studying the IFF variability, which involves multiple scales in its dynamics. In this sense, the IFF problem provides a good opportunity to demonstrate the capabilities of MS-EVA. We will see how this works in the following application.

### 3. IFF variability and scale window determination

An MS-EVA application begins with a determination of scale windows. In general, the IFF varies on a variety of scales, both in time and space. By studying the variability, the large-scale, mesoscale, and submesoscale windows are separated out. Potential ambiguities are resolved in a sensitivity study attached in the appendix.

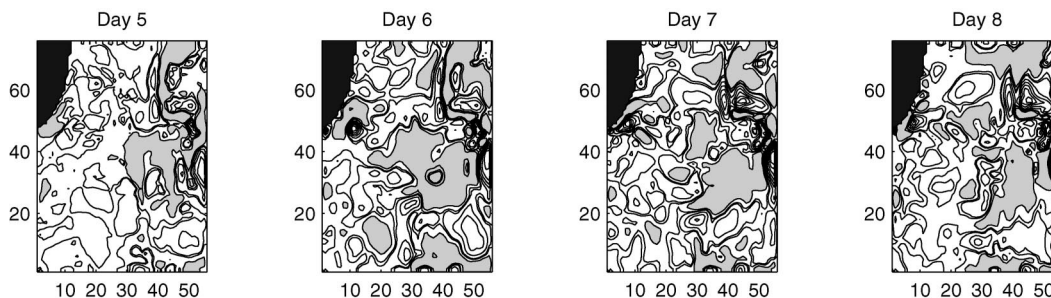


FIG. 4. The (total) buoyancy conversion rate  $b = (g/\rho_0)w\rho$  for the 300-m level from day 5 (19 Aug) to day 8 (22 Aug). Shaded is the positive  $b$  region, where the conversion is from kinetic energy to available potential energy. (White indicates negative  $b$ .) The cluster of contour lines in the northeast marks large variations of  $b$  corresponding to the abrupt change in bottom topography. The contour interval is  $1 \times 10^{-6} \text{ m}^2 \text{ s}^{-3}$ .

### a. Time variability

We study the IFF time variability through a discrete wavelet spectral analysis (cf. Kumar and Foufoula-Georgiou 1997), as scale windows are defined in LR1 on the basis of orthonormal wavelets. Here a (time) wavelet spectrum, or simply spectrum, means the “energy”<sup>1</sup> of a time series unfolded in the time-scale level plane. We have studied several typical point series and found that three of them are enough to tell the story. These points, labeled 1–3 on the bottom topography map of Fig. 1, are located at places representative of the meandering activities. The series extracted has 1024 time steps (the highest scale level  $j_2$  is hence 10), with a time interval  $\Delta t = 1800 \text{ s}$ . (They are obtained by sampling the filtered forecast output; see section 4.) The whole time span is thence  $1024 \times 0.5 \text{ h} = 21.3 \text{ day}$ , from day 0 to day 21.3. Recall the deep-sock meander is observed on day 8. We limit our discussion to the period from day 2 through day 10. The initialization stage (before day 2) and the period after day 10 are not of concern.

First look at the temperature signals. Graphed in Figs. 5a and 5b are the natural logarithm of energy as a function of time and scale level for points 1 and 2 at level 7 (300 m). In these spectra, the effect of scale windowing is apparent. A gap exists between the duration scale and smaller scales. The three spikes, located at days 2, 4, and 5, mark the instants when data are assimilated (see Liang 2002, chapter 5). It is seen that the data assimilation conspicuously affects processes with scale level higher than or equal to 5 (approximately  $21.3/2^5 \approx 0.7 \text{ day}$ ); on larger scales, the adjustment is also seen, but the flow stays qualitatively the same. In Fig. 5b, there is an obvious peak at  $j = 2$  from the beginning to day 10 and beyond, which corresponds approximately to a scale of  $21.3/2^2 = 5.3 \text{ days}$ . This peak is seen on the spectra for all depths in the water column, and is especially clear in surface layers (figures not shown). On about day 5.3, a new scale emerges in the spectrum

in the upper and middle layers, which has a scale level  $j = 3$  ( $\sim 2.7 \text{ days}$ ). Correspondingly the amplitude at scale level  $j = 2$  decreases, implying some energy transfer at this juncture. This phenomenon is also found in the spectrum for point 1 (Fig. 5a). In this case, the peak shifts from  $j = 2$  (5.3 days) to  $j = 3$  (2.7 days), then dominates the spectrum until day 10.7, though after day 8 it apparently weakens.

While the spectrum for temperature contains information about multiscale potential energy, the spectrum for velocity is related to kinetic energy. Figures 5c–e show a selection of spectra for the zonal and meridional components of velocity  $u$  and  $v$  at points 1, 2, and 3, respectively. A conspicuous feature on these maps is the maxima of the variability (above the duration scale level) at  $j = 1$  and  $j = 3$  (or sometimes  $j = 4$ ), corresponding to scales of 10.7 days and 2.7 days (or 1.3 days). Another feature is that the velocity field is very energetic in the submesoscale window. This is especially conspicuous in the spectrum of  $v$  at point 3 (Fig. 5e), where an obvious peak exists at  $j = 6$  (0.33 day) virtually all the time. Another difference between temperature and velocity is that, in the velocity spectrum, the energy maximum at  $j = 3$  generally exists before day 5.3. It is not a new emergence at that time, though it is enhanced during the meandering period, as is shown in Fig. 5e. In Fig. 5c, a significant amount of energy goes to  $j = 4$  during day 6.7–9.3, making it an apparent peak. This process spans right over the intrusion event, lasting for about 2.7 days, but it is much weakened after the meander matures (day 8).

In summary, the time variability of the IFF observed in the 1993 cruise occurs mainly on two scales: One is of 10.3 days, and the other includes a range from 1.3 to 5.3 days. While the former process is more or less uniformly distributed over the event span in the region of concern, the latter generally varies from time to time and from location to location. During day 2–10, a peak has been identified at  $j = 2$  (5.3 days) and  $j = 3$  (2.7 days), and sometimes  $j = 4$  (1.3 days), on the spectra for both temperature and velocity. These identified scales are in agreement with the estimates by Willebrand

<sup>1</sup> The term “energy” here refers to the square of the wavelet transform coefficients with the basis built in Liang (2002, chapter 2).

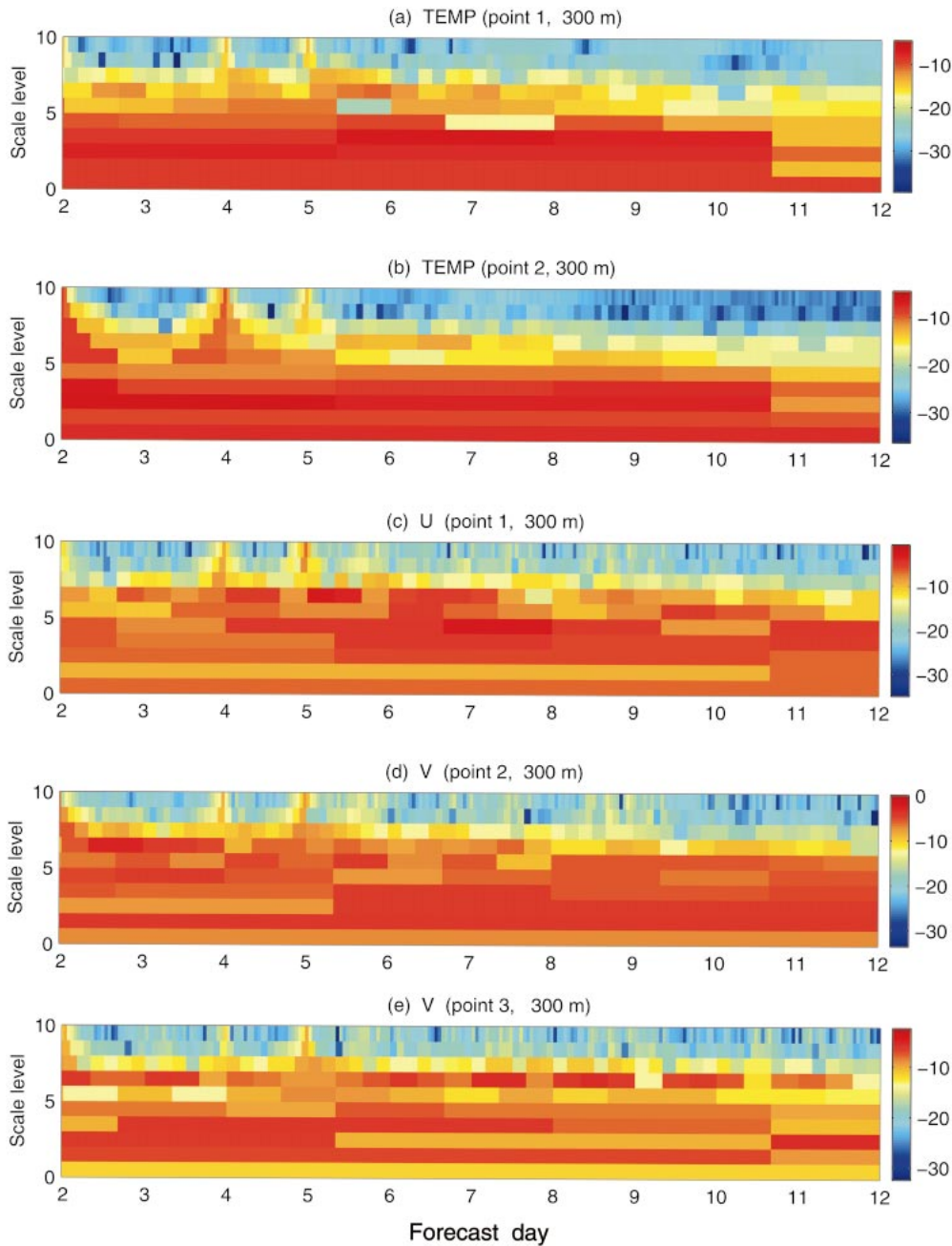


FIG. 5. Time spectra for the series at a selection of points for the deep level (300 m). Shown in each plot is the logarithm of energy instead of energy itself as a function of forecast day and scale level.

and Meincke (1980) and Hansen and Meincke (1979) (2–5 days), but a little larger than the observation (2–4 days) by Allen et al. (1994).

*b. Time window determination*

Based on the spectral analysis results, the time window bounds  $j_0$ ,  $j_1$ , and  $j_2$  are now determined. In the spectrum, the highest scale level is 10, as the signals are output at  $1024 = 2^{10}$  time points. The value of  $j_2$

hence must be 10. The setting of  $j_1$  is also straightforward. We have identified two ranges of scales, one peaked at  $j = 1$  (10.3 days) and another varying from  $j = 2$  to  $j = 4$  (1.3–5.3 days). Level  $j_1$  may be then set to be 5 to take in the event  $j = 4$  (1.3 days). Note here we have used the fact that, in a multiresolution analysis, the function space formed with a scaling basis with level  $j$  contains features with scale levels up to  $j$  but not including  $j$ .

For  $j_0$ , which demarcates the boundary between the

large-scale and mesoscale window, the setting is a little complicated. On the spectrum, clearly  $j = 1$  is not what we want for the short-term intrusion event. It should be put into the “large-scale” window, though its length is typical of a synoptic scale. But what about the other peak, which may occur either at  $j = 2$ , or at  $j = 3$  and  $j = 4$ ? A natural and reasonable choice is to put them together to make a “mesoscale” window. In that case, we have a  $j_0 = 2$ . The problem is, however,  $j = 2$  corresponds to a scale of 5.3 days, which might be a little too long if we want to focus just on the sudden cold tongue intrusion. To illustrate, go back to Fig. 3. Observe that the surface meandering begins to emerge roughly between day 5 and day 6 and is fully developed as of day 8. So it is an event occurring on a scale less than 5 days. Level  $j = 2$  is therefore out of the mesoscale window of interest, and we should choose  $j_0 = 3$ .

To summarize, the time window bounds for the deepsock intrusion study are set to be  $j_0 = 3$ ,  $j_1 = 5$ , and  $j_2 = 10$ . We have tested these bounds against sensitivity (see the appendix) and, later on in this section, we will show with an example that this is indeed a satisfactory combination.

### c. Horizontal variability

In addition to time variability, we also need information for the space window decomposition. Again, spectral analysis will help to supply the information. The spatial spectrum differs from its temporal counterpart in that more than just one dimension is involved. Here we consider only horizontal variability, so the 2D basis developed in Liang (2002) is utilized. We continue to use  $j$  to denote scale level. In case of confusion with the usage for time-scale analysis, a superscript “sp” is adopted (e.g.,  $j^{\text{sp}}$ ). Remember that the model domain is a  $140 \text{ km} \times 190 \text{ km}$  rectangle discretized into  $56 \times 76$  meshes ( $57 \times 77$  grid lines). We first interpolate the data on a  $64 \times 64$  square, which implies a maximal scale level  $j_2^{\text{sp}} = 12$  (because  $2^{12/2} = 64$ ), then remap the results back to the original grid. Given a scale level  $j^{\text{sp}}$ , the scale then ranges from  $140/\sqrt{2^{j^{\text{sp}}}}$  km to  $190/\sqrt{2^{j^{\text{sp}}}}$  km. For simplicity, we choose the average,  $165/\sqrt{2^{j^{\text{sp}}}}$  km, for our description. As in the 1D case shown in Fig. 5, the 2D wavelet transform also has a resolution problem (the lower the scale level, the coarser the resolution). In order for the energy obtained to be comparable point by point on the horizontal plane, we replace the the wavelet transform for level  $j^{\text{sp}}$  by the multiscale window transform with bounds  $j^{\text{sp}}$  and  $j^{\text{sp}} + 1$  (see LR1). As in the preceding section, it is the natural logarithm of energy instead of energy itself that is graphed for the spectrum.

We present the variability for day 7, on which the mesoscale energy has been shown to be the strongest (see subsection *e* below). The spectrum for the 300-m temperature is displayed in Fig. 6, each map corresponding to a scale level  $j^{\text{sp}}$ . Apparently, the energy

distribution differs from location to location on the horizontal plane. In this study, only the meandering intrusion region (roughly the rectangle  $I = 10 - 40$ ,  $J = 10 - 45$ ) is considered.

A conspicuous feature of Fig. 6 is that there exist a couple of maxima on the spectrum for  $j^{\text{sp}} > 0$  within the region of interest. This is to say, the IFF variability does not occur at a single scale level during the intrusion event. In a small rectangular region  $I = 20 - 40$ ,  $J = 30, 40$ , the largest variability takes place on the maps for  $j^{\text{sp}} = 3$  and  $j^{\text{sp}} = 5$ , though the latter has a more limited energetic region. This structure could be seen more clearly if the logarithm of energy is unfolded on the  $I-j^{\text{sp}}$  plane. Attached beneath the spectrum in Fig. 6 is such a plot for the zonal section  $J = 35$ . The basin scale level  $j^{\text{sp}} = 0$  is placed at the bottom and shown above is the variability, which obviously takes a double-peak form, from the western boundary all the way through  $I = 40$ . In general either of these peaks takes place on the same scale level, though we do see switches from 3 to 4 and from 5 to 6, and so on.

We have also studied spectra for other days and locations and found similar results. Evidently, the IFF variability in the intrusion region occurs mainly at two horizontal scale levels: One is  $j^{\text{sp}} = 5$  or 6, and the other is  $j^{\text{sp}} = 3$  or 4. The horizontal scales are approximately 20–30 and 40–60 km, respectively. This double-peak structure generally agrees with the observation by Allen et al. (1994), but the gap between these two scales in their estimates, 15–17 and 60–70 km, is a little larger than in the present study.

### d. Space window determination

In this study, we consider only the large-scale space window bound  $j_0^{\text{sp}}$ , as it is the local averaging that is essential to instability analysis (LR2). According to the spectrum presented above, we choose  $j_0^{\text{sp}} = 5$ . The large-scale space window thus constructed is large enough to encompass all the mesoscale variability with  $j \geq 5$ , while leaving the features with  $j < 5$  untouched. We will see later on in the appendix that the MS-EVA result is not sensitive to  $j_0^{\text{sp}}$  whenever the large-scale time window is chosen appropriately.

### e. Temperature variance of the intrusion event

We present an example to show how these time and space window bounds well characterize the IFF variability. Contoured in Fig. 7a is the temperature for the 300-m depth from day 5 through day 7 reconstructed both on the large-scale time window and large-scale horizontal window. (Only one map is presented, as they are almost the same over the duration.) Figures 7b–d are a sequence of the time mesoscale temperature “energy” (not multiplied by the factor  $2^{j_2}$ ) followed by a large-scale space synthesis. From these figures we see

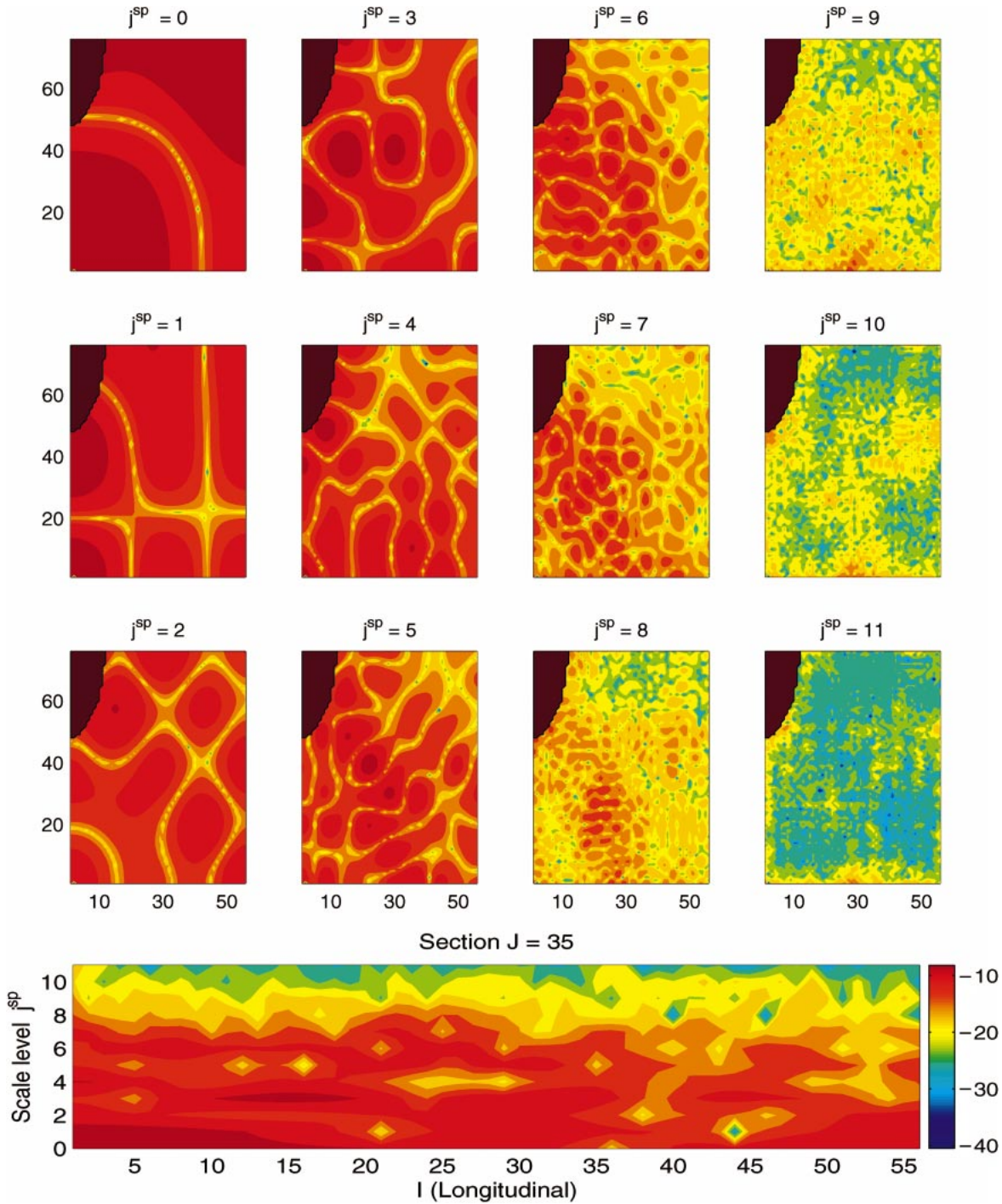


FIG. 6. Space spectrum for the 300-m temperature on day 7. Each map corresponds to a scale level as indicated in the subplot title. The  $x$  and  $y$  axes for these maps are grid indices  $I$  and  $J$ , respectively. Graphed in the maps are the logarithms of energy, and shown at the bottom is the spectrum along  $I$  on section  $J = 35$ . All maps use the same color bar.

that the mesoscale energy is small on day 5, but after that it begins to grow. An explosive growth appears on day 7 in the intrusion center. Put in another way, out of the background field (as shown in Fig. 7a) we see a

burst of mesoscale energy just before the intrusion matures. Our choice of window bounds thus allows us to separate out a process with a clear dynamical signature. We will show what it is in section 5.

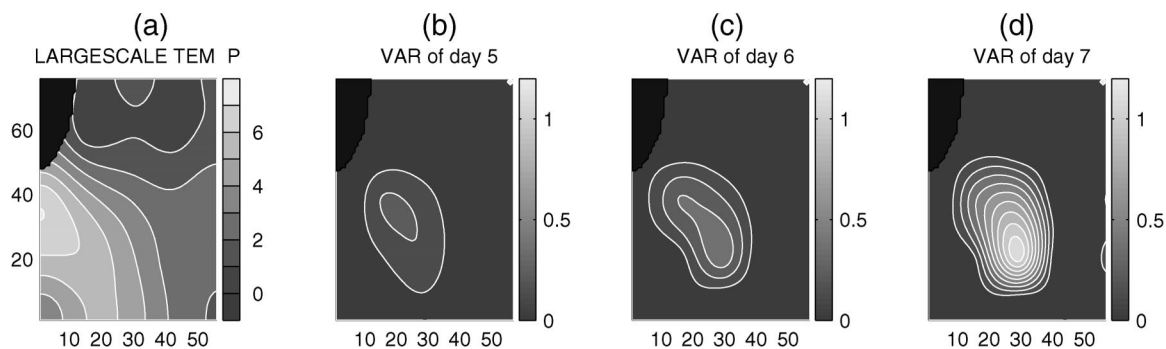


FIG. 7. (a) Background temperature (units:  $^{\circ}\text{C}$ ) reconstructed on the space–time large-scale window for the 300-m level from 19 (day 5) through 21 Aug (day 7). (The large-scale feature does not change much over this duration.) (b)–(d) Temperature variance [ $\times 10^{-3} (^{\circ}\text{C})^2$ ] on a mesoscale time window followed by a large-scale synthesis in space.

#### 4. MS-EVA setup

The MS-EVA setup includes a preparation of the background density profile, and projection of data onto the model grid. We first interpolate linearly all the field variables defined on the  $\sigma$  coordinate (section 2) onto nine  $z$  levels: 7.5, 25, 47.5, 80, 125, 190, 300, 500, and 780 m. The stationary background density profile  $\bar{\rho}(z)$  is then calculated by averaging through all the interpolated density data. The result is plotted in Fig. 8 (left). Also plotted are  $s = -\partial\bar{\rho}/\partial z$  and  $d \log s/dz$ , as functions of the vertical coordinates  $z$ . The profile  $s = s(z)$  is related to the Brunt–Väisälä frequency for the available potential energetics, and  $d \log s/dz$  is involved in the transfer term  $TS_{A_t}$  in the APE equation.

An issue arises when computational expense is concerned. It is impractical to handle the huge files of energetics because of memory limits and CPU efficiency. (On our ULTRA-10 Sun microsystem, an IFF simulation with 1024 time steps will generate a file 1.75 gigabytes in size.) On the other hand, we actually do not need simulation outputs for all the model time steps unless processes of the time step size are of concern. We therefore sample the model data to form the MS-EVA input. The sampling, however, cannot be performed directly on the model output. The underresolved time modes must be prefiltered, or aliasing could arise. In this study, the original model output has a time step of 180 s. We first apply the cubic spline scaling transform constructed in Liang (2002, chapter 2) to filter out the features with

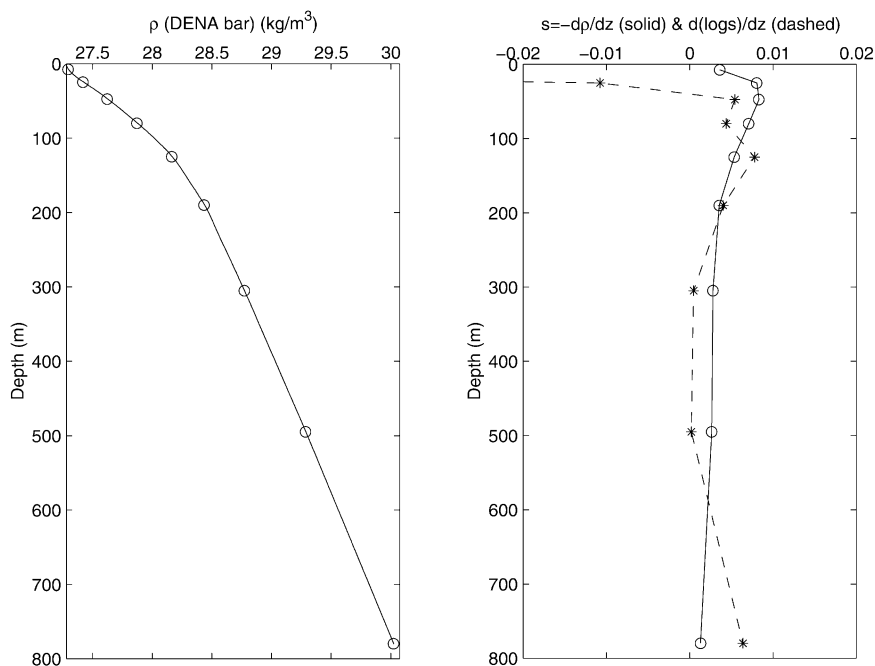


FIG. 8. The stationary density anomaly and its derived properties,  $s = -\partial\bar{\rho}/\partial z$  and  $d \log s/dz$ , as functions of  $z$ . The circles (and stars) mark the nine  $z$  levels where the MS-EVA is to be applied.

scales smaller than 10 step sizes, and then sample every 10 time steps. We set the number of series steps to be 1024 ( $j_2$  is hence  $\log_2 1024 = 10$ ). The resulting MS-EVA series thus spans 21.3 days, with a time step of 1800 s. Other parameters are listed in Table 2.

### 5. Localized instability analysis

With the MS-EVA-based localized stability theory developed in LR2, it is now possible to see how the mesoscale frontal meandering intrusion emerges out of a more slowly varying background system. Figure 9 is a time sequence of the 300-m level baroclinic instability indicator BC that is, the total transfer of available potential energy from the large-scale reservoir to the mesoscale window [see Eq. (5)]. The barotropic instability indicator BT has also been computed for days 3–8, but it is not significant at this depth and hence is not shown here. According to the criterion reviewed in the introduction, at this depth BC dominates BC + BT and hence it alone determines the instability characteristics. From Fig. 9, there is a clear “hotspot” of positive BC, which is present<sup>2</sup> on day 3, then propagates eastward, intensifies, and eventually breaks up. The timing of the breaking (day 8) corresponds exactly to the maturing of the observed intrusion. According to the localized stability theory by LR2, the system is undergoing a baroclinic instability around the growing intrusion. Underlying the complicated IFF variability, the dynamics thus turns out to be very simple.

If examined closely, more can be learned about the BC evolution. Originally, the hotspot sits near the western boundary (day 3), with a rather weak transfer. The disturbance grows and the maximal transfer rate increases from  $1.0 \times 10^{-7}$  on day 3 to  $1.5 \times 10^{-7} \text{ m}^2 \text{ s}^3$  on day 4. Beginning day 4, the controlling dynamics seems to be changed. The center of transfer travels from (10, 30) to (20, 30) (cf. point 2 in Fig. 1) from day 4 to day 5, keeping the transfer rate conserved during the evolution. Upon arriving at point 2, the center stops moving, and the transfer begins to grow again. To quantitatively measure the growth rate for the 300-m level disturbance, we integrate BC over the region where the process takes place, and multiply them by  $\rho_0 = 1025 \text{ kg m}^{-3}$  and  $\Delta x \Delta y$ . (The integration is straightforward since the region is where BC takes positive values.) The result is given in Table 3. From it we find that the variation of the gross transfer is characterized by two “steps” on the curve of growth rate versus time. The first step lies in the interval from day 4 to day 5, where the gross transfer is maintained at a level of  $2.5 \times 10^5 \text{ J m}^{-1} \text{ s}^{-1}$ . Another step is over days 6–7. The gross transfer also does not change because of the spread of the disturbance regime, albeit the maximal BC reduces by almost  $0.5 \times 10^{-7} \text{ m}^2 \text{ s}^{-3}$  over this period.

The hotspot translation in the interval of days 4–5 has a profound implication for the baroclinic instability occurring there: Disturbances grow while traveling eastward along the front but are eventually swept away downstream. This kind of instability has been called *convective instability* in fluid dynamics,<sup>3</sup> in distinction to another class of instability, *absolute instability*, which is strong enough to counteract the propagation and is manifested by growth of disturbances in all directions from its center. The concept of absolute and convective instabilities was introduced by plasma physicists and was first used for GFD studies by Thacker and Merkin (see Landau and Lifshitz 1981; Huerre and Monkewitz 1990; Pierrehumbert and Swanson 1995). A convective instability is extrinsic to local dynamics. It is generally sensitive to external forcing, acting as a noise amplifier in open flows. The development of a mixing layer between two fluids is a good prototype. In contrast, all absolute instabilities have intrinsic causes. They belong to a class of closed flow mechanisms.

With this concept the baroclinic instability manifested in Fig. 9 can be further clarified. Originally, disturbances are limited within a small region near the western boundary. A convective instability is then invoked and these disturbances are carried downstream along the front into the interior domain, triggering a spatial amplification. The whole frontal system now functions as a noise amplifier, a scenario which has also been identified by Thacker (1976) in the Gulf Stream. After day 5, the transfer center seems to be fixed at point (20,30). The baroclinic instability occurring at this stage is absolute that is, the system now behaves as a closed flow. The dynamics is locally intrinsic, and the disturbances evolve on their own, without requiring forcing from upstream any more. On day 8, all these processes break up, marking the maturing of the meandering intrusion.

An interesting question is why the convective/absolute instability transition occurs after day 5. This could be related to the amplitude of the mesoscale energy fueled by the convective instability. Our preliminary experiments (Liang 2002) indicated the sensitivity of the process to horizontal filtering, which substantially affects the spatial growth and the final meandering intrusion. It would be of both theoretical and practical interest if a definitive selection criterion of time and location of the transition could be determined in relation to the amplitude.

The convective instability works in tandem with advection and wave propagation. Advection is of some importance, as we will see soon in the next section from the distribution of  $\Delta_h Q_{A_h}$  in Fig. 10. An observation is that, in this region the velocity along the front is only about  $10 \text{ cm s}^{-1}$ , while the transfer center moves at a speed of at least  $25 \text{ km day}^{-1}$  or  $30 \text{ cm s}^{-1}$ . So wave

<sup>2</sup> The simulation has not been fully initialized until day 2. We do not use data before day 3 for process analysis.

<sup>3</sup> The term “convective instability” may have been used differently in atmospheric science. Our usage is standard in fluid dynamics and should not be confused with it.

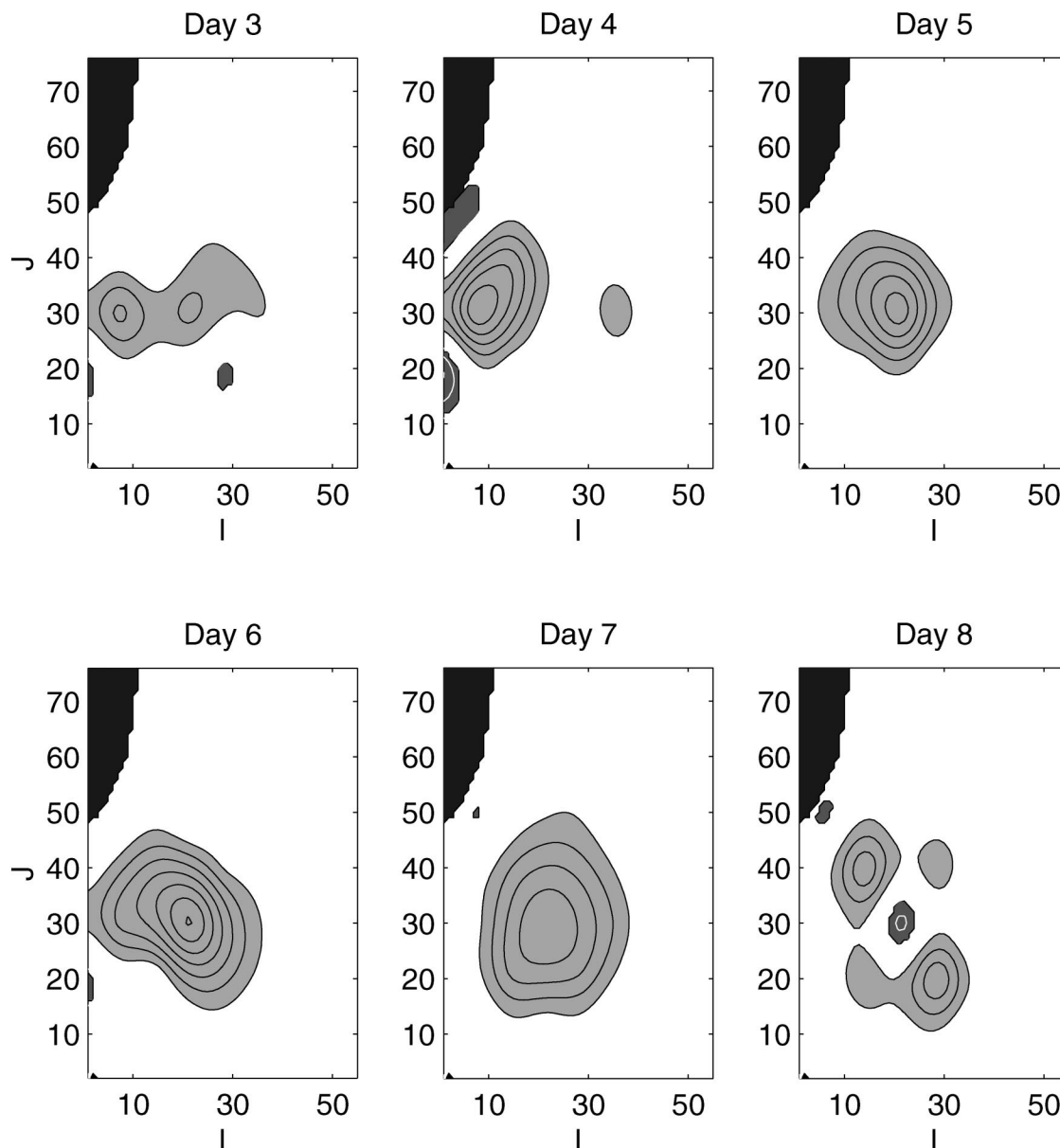


FIG. 9. Baroclinic instability indicator BC ( $\text{m}^2 \text{s}^{-3}$ ) at level 7 (300 m) from day 3 (17 Aug) through day 8 (22 Aug). The contour interval is  $2.5 \times 10^{-8}$ . Shaded indicates the nonzero BC region (positive if lightly shaded and contoured with black solid lines, otherwise negative). The black at the top-left corner indicates ocean bottom.

propagation must be more responsible for the shift than advection. If one looks closely at the BC for days 4 and 5, the two centers are oriented in two different directions and, in fact, a series of orientation changes has been identified during this period (figure not shown). This oscillation indicates that there exists a propagation of energy, whose period is estimated to be roughly 4 days.

TABLE 3. Gross energy transfer rate at level 7 ( $\times 10^5 \text{ J m}^{-1} \text{ s}^{-1}$ ).

Day 3	Day 4	Day 5	Day 6	Day 7
1.6	2.5	2.5	4.0	4.0

It would be of interest to learn more about its dispersion property, but that is beyond the scope of this study.

## 6. Energetic balance study

We have identified a baroclinic instability in the deep layer around the IFF cold tongue intrusion. We have also seen how this instability occurs. As a significant event, it must have left behind many footprints in the energetic structures. In this section, we will show how these signatures back up the existence of the event. We will first present a point series, then the balance at 300-

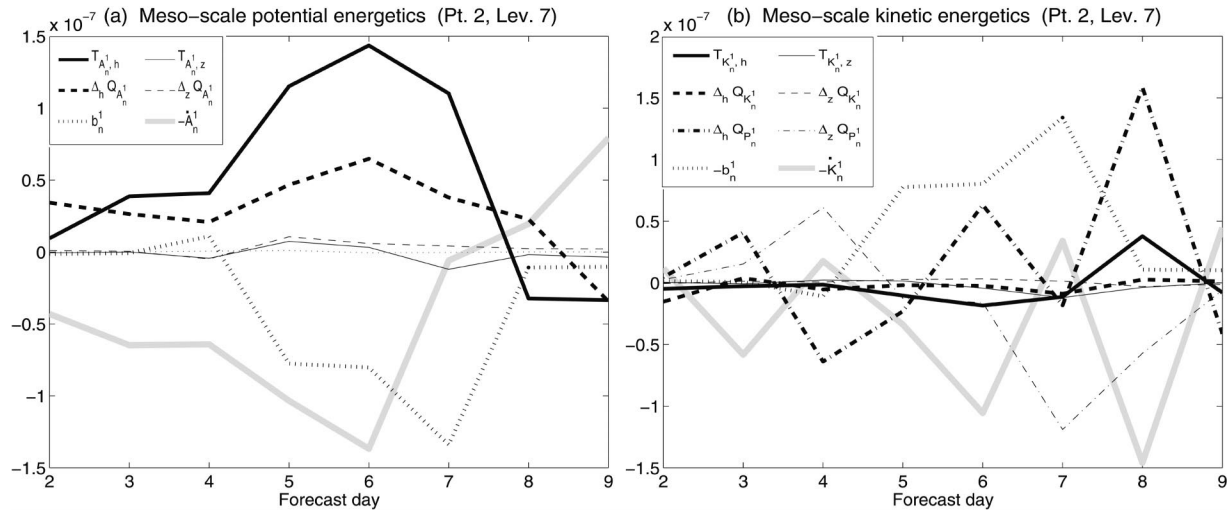


FIG. 10. Mesoscale (a) potential energy balance and (b) kinetic energy balance for point 2 (20,30) at the 300-m level (units:  $m^2 s^{-3}$ ). Refer to Table 1 and LR1 for the meanings of the MS-EVA terms.

m because this level displays the strongest dynamical information, and finally a vertical section distribution.

a. Point energetic balances

Figure 10 is the time evolution of the 300-m mesoscale APE and KE terms for point 2 in Fig. 1 (center of the day-7 hotspot in Fig. 9). In general, the APE balance (Fig. 10a) is between  $-\dot{A}_n^1$ , buoyancy conversion  $b_n^1$ , and transfer  $T_{A_n^1,h}$ , horizontal transport  $\Delta_h Q_{A_n^1}$ . [Refer to Eqs. (2) and (4) and Table 1.] For specific days, the balance may vary. Referring to Fig. 9, the baroclinic instability has been limited to the left of point 2 until day 4. Reflected in Fig. 10a is that  $b_n^1$  is not significant by this day. Note  $\Delta_h Q_{A_n^1}$  is always positive, implying that advection at this stage helps move in mesoscale energy from ambient regions. After day 4, the buoyancy conversion becomes increasingly important, and culminates on day 7, just prior to the day when the intrusion matures. During the period of days 4–8,  $b_n^1$  is negative, indicating a conversion from mesoscale potential energy to mesoscale kinetic energy.

In the kinetic energy balance (Fig. 10b), the mesoscale KE varies mainly due to the horizontal and vertical pressure work  $\Delta_h Q_{P_n^1}$  and  $\Delta_z Q_{P_n^1}$ , and due to the buoyancy conversion which appears in the equation as  $-b_n^1$ . The transfer  $T_{K_n^1,h}$  might also carry some weight for some time (e.g., on day 6), but on the whole its contribution is not significant. Besides, it takes a negative sign before the intrusion, which basically excludes the possibility of barotropic instability around this point. The other terms vary from day to day. By day 4, the buoyancy conversion has not taken place, and  $\Delta_z Q_{P_n^1}$  is positive. On day 5, we know from the previous section that the instability center moves to this point. In response  $\Delta_z Q_{P_n^1}$  changes sign immediately, and by day 7, the balance has become mainly between  $-b_n^1$  and

$\Delta_z Q_{P_n^1}$ , a signature of baroclinic instability that has been shown in LR2, and whose nondecomposed was originally discovered by Pinardi and Robinson (1986) and Spall (1989).

b. Horizontal energetic structures

Figure 11 is a pictorial presentation of the mesoscale energetics for depth 300 m (level 7). For simplicity, only those terms on the major balance in Fig. 10 are presented. We first look at column (a), which displays the transfer of APE to the mesoscale window due to horizontal density gradient ( $T_{A_n^1,h}$ ). As compared with Fig. 9, it bears resemblance to the evolution of BC in pattern, trend, and strength, so the total mesoscale potential energy transfer  $T_{A_n^1} = T_{A_n^1,h} + T_{A_n^1,z} + TS_{A_n^1}$  [Eq. (4)] is approximately equal to  $T_{A_n^1,h}$ , and the baroclinic instability indicator BC dominates the interaction analysis of  $T_{A_n^1}$  [Eq. (5)].

A baroclinic instability also leaves footprints on other horizontal maps. A most conspicuous feature is that, from day 3 through day 7, the buoyancy conversion (Fig. 11b) evolves in a similar way as  $T_{A_n^1,h}$ , does except for the opposite sign at the hotspot center. Negative  $b_n^1$  indicate a conversion of APE into KE, while the high  $b_n^1 - T_{A_n^1}$  correlation indicates that the more eddy APE is gained from the background field, the more it is converted into the eddy KE. We can also speculate on the fate of the converted energy, through an examination of the vertical pressure work rate in column (e). From day 5 to day 7, around the intrusion hotspot there is a low center on the  $\Delta_z Q_{P_n^1}$  maps. A significant part of the converted energy is thereby transported upward and downward from the spot via this mechanism.

Other significant MS-EVA terms on the mesoscale energy balance include  $\Delta_h Q_{A_n^1}$  and  $\Delta_h Q_{P_n^1}$ , the horizontal APE advection rate, and the horizontal pressure work

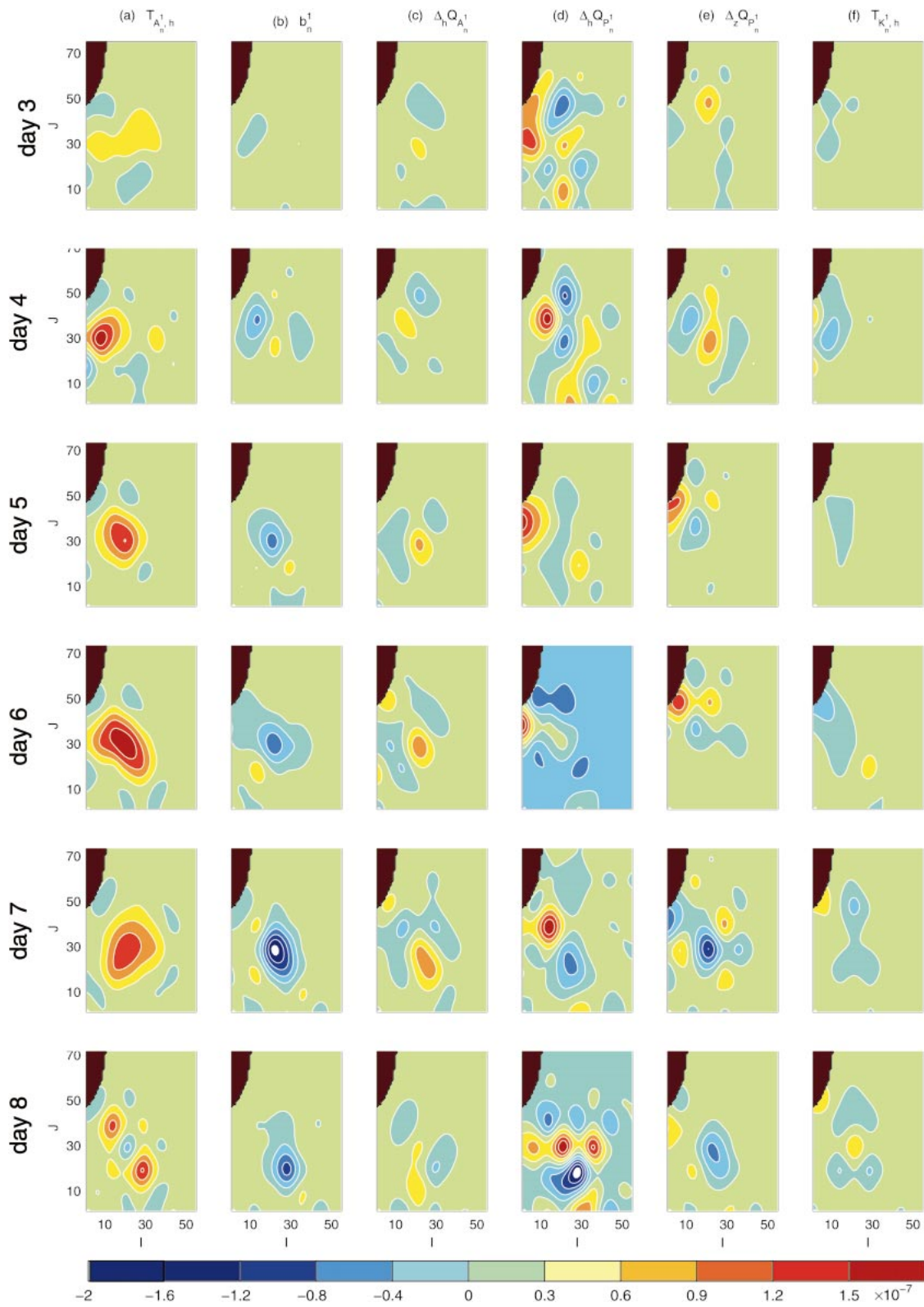


FIG. 11. Selected mesoscale MS-EVA energetics for the 300-m level. Columns (a)–(c) are the APE terms, and the rest the KE terms. Attached at the bottom is the color bar (units:  $\text{m}^2 \text{s}^{-3}$ ).

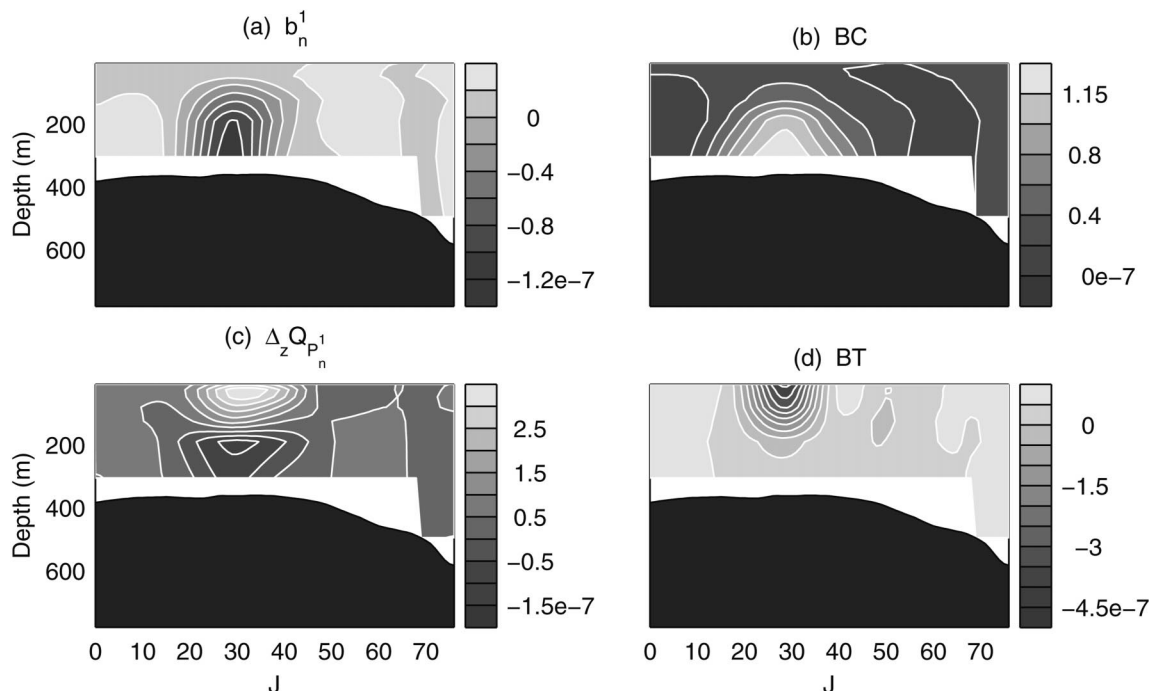


FIG. 12. Selected mesoscale energetics for day 7 on the meridional section  $I = 20$  (units:  $\text{m}^2 \text{s}^{-3}$ ).

rate. Horizontal advection is a facilitator of the convective instability. On the maps of  $\Delta_h Q_{A_n}^1$  in Fig. 11c, a positive spot exists at the transfer center with negative strips lying to the west and north, particularly to the west. This distributive pattern allows an accumulation of perturbation through advection from the west into the transfer center, fueling the absolute growth there.

The role of horizontal pressure work  $\Delta_h Q_{p_n}^1$  is not as clear as that of advection. We have speculated that it may have something to do with the propagation of the transfer hotspot. If  $\Delta_h Q_{p_n}^1$  is indeed related to some wave, it could help clarify the relation between its propagation and the convective instability, and the transition from the convective instability to the absolute instability afterwards.

Described above are the mesoscale MS-EVA distributions for the deep layer. The overall scenario is in good agreement with the previous baroclinic instability assertion. In the upper layers, the distributions are somewhat different. We see this through a vertical section study, presented next.

*c. Vertical energetic structures*

The vertical structure of the energetics allows an understanding of the extent of the dynamical processes in the water column. Since the front is not straight, we analyze a meridional section. It is chosen so as to cross the day-7 positive transfer center on the BC maps.

Figure 12 is the distribution of a selected collection of energetics on the meridional section  $I = 20$ . The two

instability indicators, BC and BT, are drawn in Figs. 12b and 12d, respectively. The other two are the buoyancy conversion  $b_n^1$  (Fig 12a) and the vertical pressure working rate  $\Delta_z Q_{p_n}^1$  (Fig. 12c), which are in the balance of Eq. (1). From the figure, the positive BC is concentrated below 150 m (approximately), and maximized at 300 m. In the upper layers (above 150 m), there is a negative barotropic transfer center between  $J = 20$  and 35, while away from that the distribution of BT is negligible. The vertical structure is particularly conspicuous in Fig. 12c. The  $\Delta_z Q_{p_n}^1$  profile near the intrusion area is separated into two regimes at roughly 150-m depth, with the lower one negative in value and the upper one positive. The negative regime corresponds to the  $b_n^1$  center and BC hotspot on the horizontal maps in Fig. 11; the positive regime indicates an accumulation of mesoscale kinetic energy which is transferred back toward the background flow (cf. the negative region of BT). According to LR2, these pictures imply the existence of an Eady-like baroclinic instability. Recall that the Eady model also shows a vertically uniform distribution for the horizontally averaged BC (see section 5 of LR2). The upward extent of BC in Fig. 12 thereby indicates that the baroclinic instability is limited below a depth of approximately 150 m.

More evidence can be found for the baroclinic instability from the tilting pattern of  $b_n^1$  and  $\Delta_z Q_{p_n}^1$ . By the Eady energetics, an unstable system has a mesoscale buoyancy conversion and a vertical pressure work both tilting with height toward the left on a vertical section with the density gradient directed away from the reader

[cf. Fig. 4.6 of Liang (2002)]. In the IFF region, the density field has a horizontal pattern which evolves generally as the temperature does (albeit more or less a compensation front), with the water from the north a little heavier than that from the south. This structure implies that, if the system is baroclinically unstable, one should see a pattern of  $b_n^1$  and  $\Delta_z Q_{\rho_n^1}$  tilting with height toward the west on a zonal section. This scenario has been reproduced exactly as expected (figure not shown). On a meridional section no general conclusion can be drawn for the pattern, as the background density distribution varies from location to location and from time to time. On day 7, the grid line  $I = 20$  happens to be near the western flank of the cold (and dense) intrusion (see Fig. 3); thus the density gradient is toward the reader. The corresponding tilting structure of buoyancy conversion and vertical pressure work then should be the opposite of that on the zonal section, if a baroclinic instability really happens. Again, this is indeed the case, as shown in Figs. 12a and 12c. Both of  $b_n^1$  and  $\Delta_z Q_{\rho_n^1}$  slope to the right (north) with height.

Evidently, the August 1993 IFF system is baroclinically unstable. The instability is Eady-like and is limited beneath a depth of roughly 150 m. The vertical energetic structure supports this assertion.

### 7. More about the baroclinic instability: Evidence from synthesized structures

We have identified a baroclinic instability in the IFF using our localized stability theory and have substantiated it with evidence from the horizontal and vertical energetic distributions. In the following, we will see that the reconstructed mesoscale structures also support this identification.

An Eady instability imprints on the vertical distribution a countertilting pattern of perturbation vertical velocity and perturbation density anomaly (see Holton 1992, p. 216). By the previous analysis, we expect the IFF variability adopts a similar structure. Here the term ‘‘perturbation’’ should be understood as the mesoscale feature. Until the end of this section, by the ‘‘mesoscale’’ feature of a given field  $p$  we mean a mesoscale time synthesis of  $p$  followed by a mesoscale space reconstruction. With this we perform a mesoscale decomposition for the vertical velocity  $w$  and density anomaly  $\rho$ . The time-scale window bounds used are the same as the standard experiment:  $j_0 = 3$ ,  $j_1 = 5$ , and the horizontal window is chosen to be  $j_0^{\text{sp}} = 3$ ,  $j_1^{\text{sp}} = 6$ , according to the analysis in section 3c.

Consider section  $I = 20$ , the meridional section, which we have examined before, and day 7, when a strong potential energy transfer has been clearly observed. Given the background density structure (gradient directing out of the paper), the mesoscale  $w$  is expected to have a pattern with phase lines sloping with height toward the east for an Eady-like baroclinically unstable process. Under the same conditions, the cor-

responding mesoscale density anomaly should also have a tilting pattern, but toward the opposite direction. This is indeed the case, as shown in Fig. 13 on the distributions of the day-7 mesoscale  $w$  and  $\rho$  in this section. The mesoscale  $w$  and  $\rho$  therefore adopt a vertical structure that supports our previous assertion. (The vertical phase structure reproduced in the simulation in section 2 could be related to this tilting, but here we do not intend to elaborate on the relation because the phasing exists mainly in the surface layer where an understanding of the dynamics requires more information.) Other structures, such as the mesoscale dynamic pressure, have also been computed, and all results reveal patterns consistent with a baroclinic instability.

### 8. Other transfers from the interaction analysis

Now the remaining issue is whether the identified baroclinic instability is the cause of the cold intrusion. In an MS-EVA with more than two scale windows, the energy released from the background could go all the way down to the small-scale window to trigger some submesoscale oscillation without leaving anything for mesoscale processes. In section 3, we have seen a significant part of energy residing in the submesoscale window on the time spectrum of  $v$  (Fig. 5e). A mere study of the transfer between two windows is apparently not sufficient. We also need to see how they communicate with the submesoscale window.

We focus on the total APE and KE transfers to the mesoscale window,  $T_{A_n^1}$  and  $T_{K_n^1}$ , which are defined in Eqs. (3) and (4), respectively. By the technique developed in LR1, every transfer term can be decomposed, according to the energy source, into a summation of four terms. The total APE and KE transfers may also be done as

$$T_{A_n^1} = T_{A_n^1}^{0 \rightarrow 1} + T_{A_n^1}^{2 \rightarrow 1} + T_{A_n^1}^{2 \oplus 0 \rightarrow 1} + T_{A_n^1}^{1 \rightarrow 1} \quad \text{and} \quad (7)$$

$$T_{K_n^1} = T_{K_n^1}^{0 \rightarrow 1} + T_{K_n^1}^{2 \rightarrow 1} + T_{K_n^1}^{2 \oplus 0 \rightarrow 1} + T_{K_n^1}^{1 \rightarrow 1}. \quad (8)$$

In the superscripts, the numbers 0, 1, and 2 represent respectively the large-, meso-, and submesoscale window, and the arrow indicates the direction of energy flow. In particular, the superscript  $0 \oplus 2 \rightarrow 1$  is used for the transfer to the mesoscale window due to the large-scale–submesoscale interaction. (The symbol  $0 \oplus 2$  indicates the large-scale window combined with the submesoscale window.) In these two equations,  $T_{A_n^1}^{0 \rightarrow 1} = \text{BC}$  dominates the eight terms on the right-hand side during the deep-layer baroclinic instability event. We redraw it for day 7 and depth 300 m in Fig. 14a, together with a distribution of the mesoscale potential energy transfer from the submesoscale window ( $T_{A_n^1}^{2 \rightarrow 1}$ ) at the same level for the same day (Fig. 14b). In Fig. 14b, there is a negative core located close to where the BC hotspot lies, implying that part of the energy transferred from the background field has been passed to the submeso-

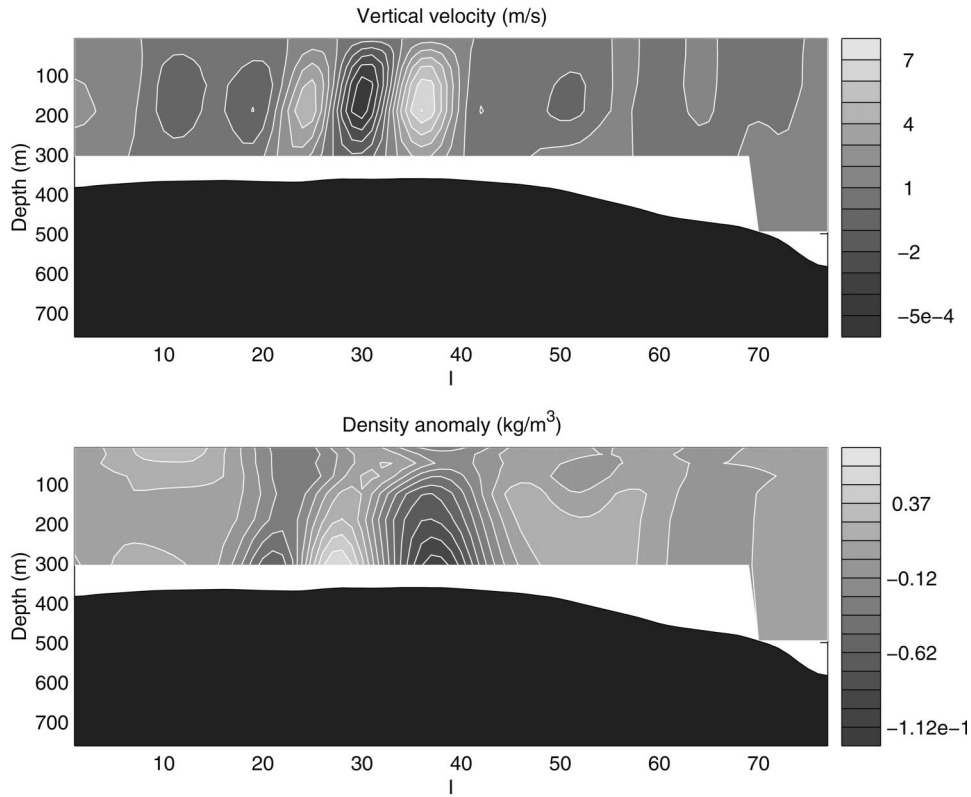


FIG. 13. The day-7 mesoscale (top) vertical velocity and (bottom) density anomaly on the meridional section  $l = 20$ . In this figure by the “mesoscale” feature of a field we mean its time mesoscale synthesis with window bounds  $j_0 = 3$  and  $j_1 = 5$  followed by a horizontal mesoscale synthesis with bounds  $j_0^p = 3$  and  $j_1^p = 6$ .

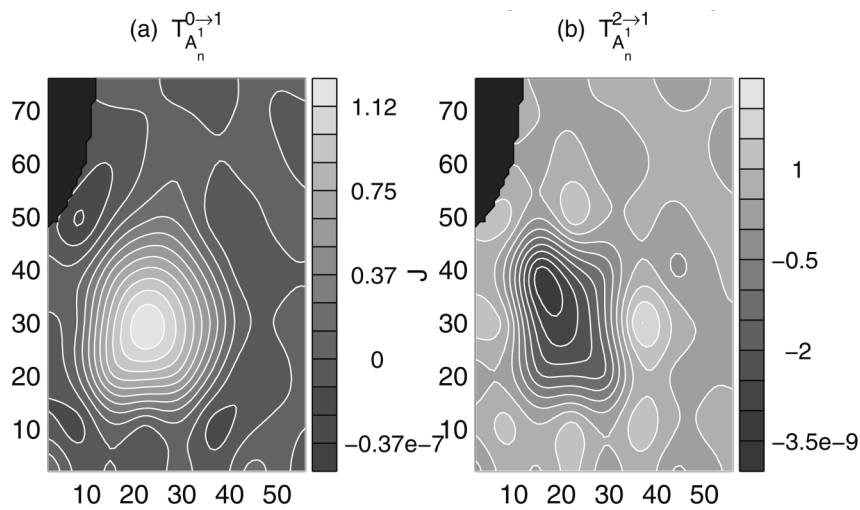


FIG. 14. Part of the interaction analysis of the day-7, level-7 (300 m) mesoscale APE transfer,  $T_{A_n} = T_{A_n, h^*} + T_{A_n, c} + TS_{A_n}$  (units:  $m^2 s^{-3}$ ). The integers 0, 1, and 2 in the superscripts represent the large-, meso-, and submesoscale windows, respectively [cf. Eq. (7)]. Drawn in (a) is simply the BC as shown in Fig. 9.

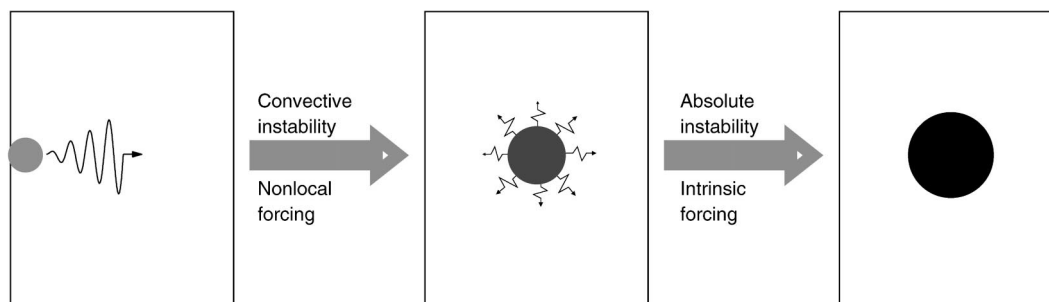


FIG. 15. A schematic summarizing the baroclinic instability processes during the IFF cold meandering intrusion.

scale window. This negative core is far from significant in comparison to the hotspot on the BC map. The baroclinic instability is therefore mainly for the mesoscale meandering intrusion.

It should be noted that the submesoscale energetics, though small in comparison with the mesoscale energetics, have their own distinct patterns. One might expect a submesoscale energy flow chart, just as that in the mesoscale window. The current dataset, however, is inappropriate for the study of submesoscale energetics because of the nonphysical high-frequency energy introduced by the data assimilation on days 4 and 5. (See the spikes in Fig. 5.) Besides, as noted in LR1, submesoscale energetics have important inputs from subgrid processes. How to incorporate subgrid process parameterization into the MS-EVA formalism is still an open question. For these reasons, we leave this submesoscale problem to future research. (The  $T_{k_i}^{2 \rightarrow 1}$  and  $T_{A_i}^{2 \rightarrow 1}$ , albeit represented with the contribution from the submesoscale window, are in the balance of mesoscale energetics.)

So far we have finished the mesoscale energetics study. The IFF system undergoes a baroclinic instability around the meandering cold intrusion, and the instability occurs below a certain depth of roughly 150 m. The energy gained from this process goes to the submesoscale disturbances as well as the mesoscale processes, but most of it stays in the mesoscale window, serving to fuel the growth of the intrusion event.

## 9. Discussion and conclusions

Using the multiscale energy and vorticity analysis (MS-EVA) and the MS-EVA-based localized stability theory, we have studied the Iceland–Faeroe frontal variability during 14–24 August 1993. The dynamical processes underlying the cold meandering intrusion have been inferred, and the inference substantiated with evidence using a variety of diagnostics.

We first studied the energy transfer from the large-scale window to the mesoscale window, which is dominated by BC, the baroclinic instability indicator. In the deep layers, BC is distributed as a solitary positive center in the study domain over the time period of concern. By the localized stability theory developed in LR2, there

is a baroclinic instability occurring around the intrusion. The energy transferred through this instability has a growing trend, and the gross growth rate reaches its maximum on days 6 and 7. After that, the process ceases and breaks up, and correspondingly the meandering intrusion matures. The whole process is limited to depths greater than roughly 150 m.

The baroclinic instability manifests itself in different forms at different stages. Originally it occurs near the western boundary. The disturbances grow spatially along the front into the interior domain. The transfer center stops on day 5 when the meandering has become powerful enough to counteract the propagation. The general scenario can be summarized as a convective instability, triggered by disturbances from the upstream, and an absolute instability, driven by some intrinsic forcing totally local to the cold intrusion. Schematized in Fig. 15 is a pictorial presentation of these processes.

The deep-layer baroclinic instability inferred from the BC distribution has been backed up by diagnosis from MS-EVA energetics and synthesized structures. For the 300-m level energetic balance, the mesoscale buoyancy conversion is distributed in a general pattern similar to that of BC except for a negative sign. The mesoscale potential energy obtained from the large-scale window is then converted into the mesoscale kinetic energy, which is further carried upward and downward through the vertical pressure work. This energetic scenario has been associated with the Eady-like baroclinic instability in LR2, and was discovered by Pinardi and Robinson (1986) and Spall (1989). The countertilting pattern of the mesoscale vertical velocity versus mesoscale density anomaly on the section across the intrusion also supports a baroclinic instability.

We have also studied how the system distributes the energy gained through the baroclinic instability. An interaction analysis reveals that, in comparison to BC, the energy leaving the mesoscale window for submesoscale processes is more than one order smaller. In other words, the energy transferred from the background flow, though going to the submesoscale window as well, indeed serves to fuel the growth of the mesoscale intrusion.

All in all, the MS-EVA offers a new way to process diagnostics, and with it the August 1993 IFF intrusion

has been interpreted from a dynamical point of view. Nevertheless, some problems remain to be solved. For example, it seems that the background system chosen for the window decomposition is also oscillating. One may want to know whether it gains its energy from some larger/longer process. If so, the cold intrusion captured in the experiment could be a second instability. This hypothesis, which requires data from before day 2, is yet to be tested with a longer simulation fully initialized prior to 16 August 1993.

*Acknowledgments.* We thank Prof. Donald G. M. Anderson, Dr. Kenneth Brink, and Dr. Arthur J. Miller for important and interesting scientific discussions. Author X. San Liang also thanks Prof. Ya-ner Bar-Yam for his inspiration from complex systems and thanks Prof. Brian Farrell, Mr. Wayne Leslie, Dr. Patrick Haley, Dr. Pierre Lermusiaux, Dr. Carlos Lozano, and Ms. Gioia Sweetland for their generous help. The intuitive comments from an anonymous reviewer about the time and location selection for convective-absolute instability transition are sincerely appreciated. This work was supported by the Office of Naval Research under Contracts N00014-95-1-0371, N00014-02-1-0989, and N00014-97-1-0239 to Harvard University.

APPENDIX

Sensitivity Study

As we mentioned in section 3, there could be some ambiguity in setting the time and space window bounds. This appendix settles this ambiguity by testing the window parametric combinations against sensitivity. We choose day 7 and depth 300 m to address this issue and focus only on  $b_n^1$  and BC, as they best elucidate the mechanism of the meandering intrusion. The related experiments are listed in Table A1.

a. Time window bounds

We have chosen a time window bound combination  $j_0 = 3$  and  $j_1 = 5$  in the standard experiment (experiment 1 in Table A1). This choice makes a mesoscale window with scale levels  $j = 3$  and  $j = 4$ . But from section 3b, this window could be enlarged with more levels included. It is not impossible to have a  $j_1$  exceeding 5, while  $j_0$  could be made smaller than 3.

We first examine the effect of an extension of  $j_1$  beyond  $j = 5$ . Given  $j_0 = 3$ ,  $j_0^{sp} = 5$ , we have tried all the possibilities with  $j_1 = 6-10$  (experiment 2). The resulting energetics are basically the same as those ob-

TABLE A1. MS-EVA experiments for the IFF variability study (W = window).

Expt	Time W			Space W	Remarks	
	Type	No.	$j_0$	$j_1$		$j_0^{sp}$
Time W expt	1	1	3	5	5	The standard experiment
	2	2	3	6-10	5	Almost the same as expt 1
	3	3	0	5	5	$b_n^1$ positive in the intrusion region
	4	4	1	5	5	Similar to expt 3
	5	5	2	5	5	Transfer information disguised on BC map
Horizontal W expt	6	6	3	5	3	Similar to expt 1 but hotspot smeared
	7	7	3	5	4	Same as expt 6
	8	8	0	5	3	Some features in expt 3 disappear

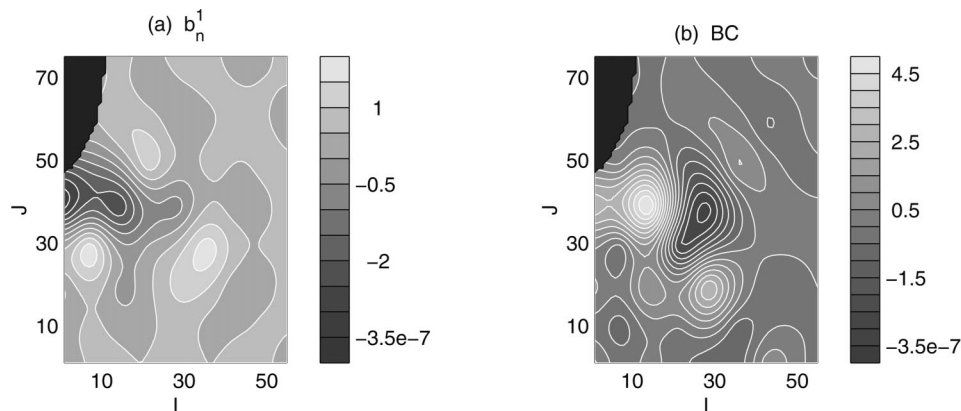
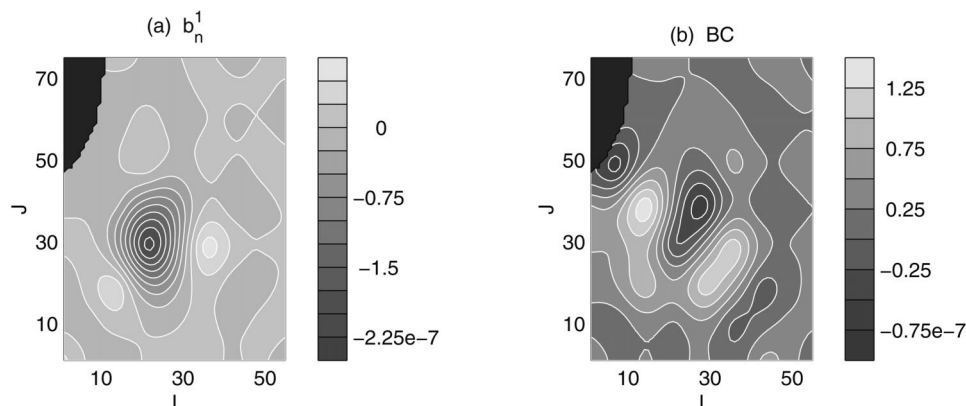


FIG. A1. Mesoscale (a) buoyancy conversion and (b) baroclinic instability indicator for the seventh day at depth 300 m, with time window bounds  $j_0 = 0$ ,  $j_1 = 5$ , and space window bound  $j_0^{sp} = 5$ . All the energetics are in meters squared per seconds cubed.

FIG. A2. As in Fig. A1 but for  $j_0 = 2$ .

tained in the standard experiment. In a word, the choice of  $j_1$  is not sensitive provided that processes with  $j = 3$ –4 are included.

The real problem of time parameters comes in choosing  $j_0$ . In addition to the standard experiment setting, we have three more options:  $j_0 = 0$ ,  $j_0 = 1$ ,  $j_0 = 2$ . Figure A1 shows the  $b_n^1$  and BC from experiment 3, with  $j_0 = 0$  and other parameters the same as the standard experiment, for the seventh forecast day at the 300-m depth. In comparison with its counterparts in Figs. 9 and 11, the buoyancy conversion  $b_n^1$  turns positive in the cold intrusion region, and a negative tongue appears between  $J = 35$  and  $J = 50$  right to the western boundary. On the BC map, the solitary hotspot is replaced by a dipole plus a positive region at a location roughly corresponding to the negative tongue on the  $b_n^1$  map. By location the correlation between the processes identified here and the intrusion event observed in the forecast is far from significant. Apparently, the addition of processes with  $j = 0, 1$ , and 2 complicates the features of interest.

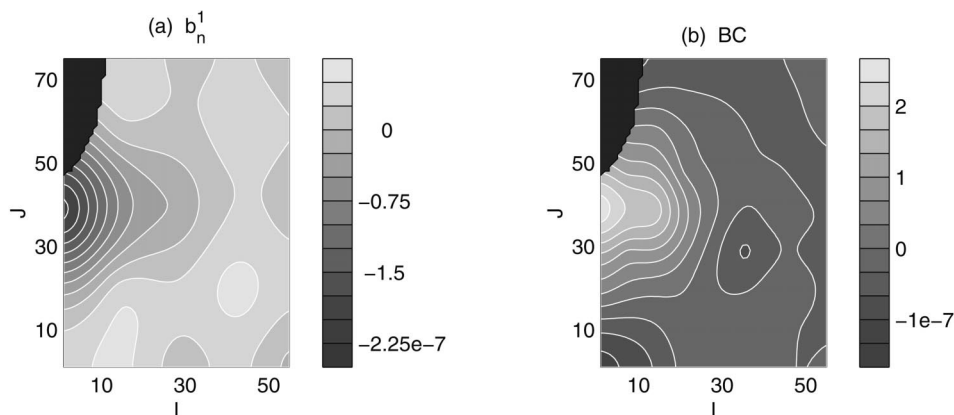
A similar result can be obtained with  $j_0 = 1$  (experiment 4), which forms a mesoscale window with the

level  $j = 1$  or scale 10.7 days included. The new features on the  $b_n^1$  and BC maps in the above observation with reference to Figs. 9 and 11 are therefore mainly from the events occurring at  $j = 1$  and 2.

Most of the  $j_0$  ambiguity arises in the case  $j_0 = 2$ , as mentioned in section 3b. In experiment 5, we set the mesoscale window according to this choice (other parameters as in experiment 1), and show the result in Fig. A2. Compared to Figs. 9 and 11 (day 7), the negative  $b_n^1$  center remains similar, but on the BC map, the conspicuous solitary hotspot is not apparent. Replaced at the same location is a negative core with some positive peripheral BC bands. In contrast to the standard experiment, a different process apparently has edged in, with an energy transfer pattern that is quite unexpected for our purpose. The scale level  $j = 2$  thus does not characterize the cold intrusion event, and hence a time window bound must be chosen such that  $j_0 > 2$ .

#### b. Horizontal window bounds

In the MS-EVA-based instability analysis, the horizontal window parameter  $j_0^H$  is not for scale decompo-

FIG. A3. Mesoscale potential energetics ( $\text{m}^2 \text{s}^{-3}$ ) for day 7 at depth 300 m with time window bounds  $j_0 = 0$ ,  $j_1 = 5$ , and the space window bound  $j_0^H = 3$ .

sition, but for local averaging. We hence expect that it should not be as essential as the  $j_0$  for the time window. In experiment 6, we run the standard experiment again, but this time with a larger horizontal window with  $j_0^{\text{sp}} = 3$ . The results, particularly the distributions for  $b_n^i$  and BC at level 7, do not exhibit fundamental change from that of experiment 1. Both the negative  $b_n^i$  center and the BC hotspot are there, though horizontally much smeared (figure not shown). This remarkable pattern still exists when  $j_0^{\text{sp}}$  is switched to 4 (experiment 7), with another peak as well as  $j_0^{\text{sp}} = 3$  identified on the horizontal wavelet spectrum. Consequently, for the standard experiment, the mesoscale MS-EVA results are insensitive to the choice of  $j_0^{\text{sp}}$ .

However, when the time window bound  $j_0$  is not correctly set, the effect of  $j_0^{\text{sp}}$  does show its influence. In Fig. A3 we regraph the  $b_n^i$  and BC obtained in experiment 3 (Fig. A1), but with a low  $j_0^{\text{sp}} = 3$ . Apparently, the negative  $b_n^i$  (positive BC) region near the western boundary is made much more clear, but the positive/negative BC pair in the middle area basically has been eliminated.

Consequently, the success of the IFF MS-EVA analysis relies on the choice of a time window bound  $j_0$  that correctly reflects the meandering intrusion. Addition of any processes with scale level below  $j = 3$  into the mesoscale window could complicate the energetics and make the dynamics intractable. When an appropriate  $j_0$  is set, the application is not sensitive to the change of the horizontal window bound.

#### REFERENCES

- Allen, J. T., D. A. Smeed, and A. L. Chadwick, 1994: Eddies and mixing at the Iceland–Faeroe front. *Deep-Sea Res.*, **41**, 51–79.
- Hallock, Z. R., 1985: Variability of frontal structure in the southern Norwegian Sea. *J. Phys. Oceanogr.*, **15**, 1245–1254.
- Hansen, B., and J. Meincke, 1979: Eddies and meanders in the Iceland–Faeroe Ridge area. *Deep-Sea Res.*, **26A**, 1067–1082.
- Holton, J. R., 1992: *An Introduction to Dynamic Meteorology*. Academic Press, 496 pp.
- Hopkins, T., 1988: The GIN sea: Review of physical oceanography and literature from 1972. SACLANT Undersea Research Center Rep. SR-124, 190 pp.
- Huerre, P., and P. Monkewitz, 1990: Local and global instabilities in spatially developing flows. *Annu. Rev. Fluid Mech.*, **22**, 473–537.
- Killworth, P., D. N. Paldor, and M. E. Stern, 1984: Wave propagation and growth on a surface front in a two-layer geostrophic current. *J. Mar. Res.*, **42**, 761–785.
- Kumar, P., and E. Foufoula-Georgiou, 1997: Wavelet analysis for geophysical applications. *Rev. Geophys.*, **35**, 385–412.
- Landau, L. D., and E. M. Lifshitz, 1981: *Physical Kinetics*. Butterworth Heinemann, 452 pp.
- Liang, X. S., 2002: Wavelet-based multiscale window transform and energy and vorticity analysis. Ph.D. thesis, Harvard University, 411 pp.
- , and A. R. Robinson, 2003a: Localized multiscale energy and vorticity analysis. Part I: Fundamentals. *Dyn. Atmos. Oceans*, in press.
- , and —, 2003b: Localized multiscale energy and vorticity analysis. Part II: Instability theory and validation. *Dyn. Atmos. Oceans*, in press.
- Miller, A. J., and B. D. Cornuelle, 1999: Forecasts from fits of frontal fluctuations. *Dyn. Atmos. Oceans*, **29**, 305–333.
- , P.-M. Poulain, A. Warn-Varnas, H. G. Arango, A. R. Robinson, and W. G. Leslie, 1995: Quasigeostrophic forecasting and physical processes of Iceland–Faeroe frontal variability. *J. Phys. Oceanogr.*, **25**, 1273–1295.
- Pierrehumbert, R. T., and K. L. Swanson, 1995: Baroclinic instability. *Annu. Rev. Fluid Mech.*, **27**, 419–467.
- Pinardi, N., and A. Robinson, 1986: Quasigeostrophic energetics of open ocean regions. *Dyn. Atmos. Oceans*, **10**, 185–219.
- Robinson, A. R., H. G. Arango, A. J. Miller, A. Warn-Varnas, P.-M. Poulain, and W. G. Leslie, 1996: Real-time operational forecasting on shipboard of the Iceland–Faeroe frontal variability. *Bull. Amer. Meteor. Soc.*, **77**, 243–259.
- Spall, M., 1989: Regional primitive equation modeling and analysis of the POLYMODE data set. *Dyn. Atmos. Oceans*, **14**, 125–174.
- Thacker, W. C., 1976: Spatial growth of Gulf Stream meanders. *Geophys. Fluid Dyn.*, **7**, 271–295.
- Willebrand, J., and J. Meincke, 1980: Statistical analysis of fluctuations in the Iceland–Scotland frontal zone. *Deep-Sea Res.*, **27A**, 1047–1066.